AIAA Meeting Papers on Disc, January 1997
A9715433, AIAA Paper 97-0368

Linear-eddy subgrid model for reacting large-eddy simulations - Heat release effects

William H. Calhoon, Jr.
SPARTA, Inc., Edwards AFB, CA

Suresh Menon
Georgia Inst. of Technology, Atlanta

AIAA, Aerospace Sciences Meeting & Exhibit, 35th, Reno, NV, Jan. 6-9, 1997

Large-eddy simulations (LES) is an attractive approach for the simulation of turbulent flows involving chemical reactions. Within LES, the large energy containing scales of motion, which are highly geometry dependent, are explicitly calculated. The smaller more universal scales of motion, however, are modeled using an appropriate subgrid model. Applying LES to reacting flows is difficult due to additional unclosed terms in the LES equations related to combustion processes. One approach for modeling these terms is to employ the linear-eddy mixing (LEM) model. This model separately treats the physical process of molecular diffusion and turbulent stirring at the small scales so that an accurate picture of the interaction of the turbulence and the chemistry can be obtained. Previous applications of the LEM model within LES have been for negligible heat release cases in which the chemistry can be uncoupled from the fluid dynamics. This paper describes the extension of the methodology to fully coupled simulations with heat release. (Author)

LINEAR-EDDY SUBGRID MODEL FOR REACTING LARGE-EDDY SIMULATIONS: HEAT RELEASE EFFECTS

William H. Calhoon, Jr.*
SPARTA, Inc.
Phillips Laboratory
Edwards Air Force Base, California

Suresh Menon†
School of Aerospace Engineering
Georgia Institute of Technology
Atlanta, Georgia

ABSTRACT

Large-eddy simulations(LES) is an attractive approach for the simulation of turbulent flows involving chemical reactions. Within LES, the large energy containing scales of motion, which are highly geometry dependent, are explicitly calculated. The smaller more universal scales of motion, however, are modeled using an appropriate subgrid model. Applying LES to reacting flows is difficult due to additional unclosed terms in the LES equations related to combustion processes. One approach for modeling these terms is to employ the *linear-eddy mixing*(LEM) model. This model separately treats the physical process of molecular diffusion and turbulent stirring at the small scales so that an accurate picture of the interaction of the turbulence and the chemistry can be obtained. Previous applications of the LEM model within LES have been for negligible heat release cases in which the chemistry can be uncoupled from the fluid dynamics. This paper describes the extension of the methodology to fully coupled simulations with heat release.

1 INTRODUCTION

Combustion processes play an important role in a wide variety of industrial applications. In many of these applications, the chemical reaction zone exists in a turbulent fluid dynamical environment. This turbulent environment may generally be characterized by highly unsteady motions of the fluid which exist on a wide range of length and time scales. For high Reynolds number flows, the time scale of the smaller turbulent motions which promote mixing of the chemical species may be of the same order as the time scale of the chemical reactions converting these species to products. Consequently, there may be a strong coupling of the turbulence and chemistry in a turbulent reacting flow.

For engineers to be successful in improving hardware design involving turbulent reacting flows requires the proper characterization of 1) the highly unsteady mixing process occurring in turbulent flows and 2) the effect of turbulence-chemistry interactions on the combustion process. Experimental investigations have been undertaken to understand and characterize turbulent reacting flows. However, experiments alone may not provide the necessary information for the design process due to the expense of conducting comprehensive parametric studies and current limitations in measurement technology. As a consequence, numerical simulations of turbulent reacting flows are necessary in order to complement the experimental results and provide additional understanding. However, designers seeking to improve combustor efficiency and reduce pollution emissions, for example, are increasingly limited by accuracy and tractability limitations of existing modeling approaches.

A promising approach for modeling turbulent reacting flows of practical interest is large-eddy simulation (LES). The underlying philosophy behind LES is to explicitly calculate the large energy containing scales of turbulent motion which are directly effected by boundary conditions while only modeling the smaller scales of the flow. The large scales are difficult to model due to their variability from one problem geometry to the next. The smaller scales are presumed to be more universal in nature and, therefore, more amenable to successful modeling. The LES equations of motion describe the evolution of the large scales and are derived by applying a *spatial* filter function to the gas-phase, Navier-Stokes reacting flow equations. This filtering process separates out the effects of the highly geometry dependent large scales from the more universal small scales. The filtering results in a set of equations describing the evolution of the large scale or resolved part of the flow variables. The effect of the small unresolved scales appears as additional unknown subgrid terms in the resolved field equations. These subgrid terms must be modeled or additional equations for these terms derived in order to close the equation set.

Subgrid-scale (SGS) models for the application of LES to nonreacting, compressible flows have been developed (Erlebacher et al., 1990; Moin et al., 1991; Menon, 1991). However, relatively few extensions to reacting flows have been made, since additional closure problems arise from combustion related terms which are difficult to model. These additional terms include: 1) the filtered reaction source terms, 2) the terms describing species transport due to turbulence and 3) the temperature-species corre-

*Staff Scientist, Member AIAA, formally at Georgia Tech.
†Associate Professor, Senior Member AIAA.

lations arising in the state equations.

LES of reacting flows has been previously applied to both premixed (Menon and Jou, 1991; Smith and Menon, 1994; Menon *et al.*, 1993a; Fureby, 1995; Fureby and Möller) and nonpremixed (Schumann, 1989; Sykes *et al.*, 1992, 1995; Frankel *et al.*, 1993; Gao and O'Brien; 1993; Koutmos *et al.*, 1996) combustion. Common in many of these applications is the use of the gradient diffusion assumption (Tennekes and Lumley, 1972) to model the species transport terms due to turbulence. Use of this type of assumption for reactive species is dubious, as noted earlier (Dimotakis, 1989; Pope, 1979).

An alternative subgrid modeling approach which avoids using this assumption has been proposed by Menon *et al.* (1993b) and McMurtry *et al.* (1992). They investigated the application of Kerstein's *linear-eddy mixing* (LEM) model (Kerstein, 1988, 1989, 1990, 1991 1992) as a subgrid model in LES of turbulent premixed and diffusion flames. The LEM model used in these calculations separately treats the physical process of molecular diffusion and turbulent stirring at the small scales so that an accurate picture of the interaction of the turbulence and the chemistry can be obtained. Menon *et al.* (1993b) and McMurtry *et al.* (1992) demonstrated the good *qualitative* characteristics of this approach. Calhoon and Menon (1996) refined the model and applied it to reacting mixing layers above the mixing transition. Their investigation demonstrated excellent *quantitative* comparison with experimental results for 1) mean product across the layer, 2) mean mixed fluid across the layer, 3) decay of integrated product with Reynolds number and 4) variation of integrated product with Damköhler number. Mathey and Chollet (1996) have also applied the LEM approach to a 3-D LES simulation of a reacting mixing layer with no heat release. However, all of the previously mentioned applications of the LEM subgrid model were for cases in which the chemistry was uncoupled from the fluid dynamics.

This paper describes the application of the LEM subgrid model for fully coupled LES simulations of turbulent diffusion flames with heat release.

2 LES SIMULATION MODEL

The LES reacting flow equations are derived by the convolution of a spatial filter function with the Navier-Stokes equations describing mass, momentum, energy and species conservation for a multi-component fluid. The filtering results in a set of equations for the large scale or resolved part of the flow variables. The resolved part of any variable M which varies in space x_j and time t is defined by the convolution,

$$\overline{M}(x_j,t) = \int_{\Xi} M(z_j,t)G(x_j - z_j)dz_j \qquad (1)$$

where G is the spatial function which has a characteristic width Δ_{LES}. In this study, the *box* filter is used so that Δ_{LES} is equal to the computation grid cell width. For compressible flows, it is customary to introduce mass weighted or Favre filtering (Erlebacher *et al.*, 1990) and express the resolved field as $\widetilde{M} = \overline{\rho M}/\overline{\rho}$. The turbulent field variable M can now be decomposed into the resolved and unresolved parts as $M = \widetilde{M} + M''$, where M'' is the unresolved or fluctuating subgrid component.

Applying the filtering defined in equation (1) to the governing equations results in the LES equations of motion for reacting flows. These equations describe the temporal and spatial evolution of the resolved variables $\{\bar{\rho}, \bar{\rho}\tilde{u}_j, \bar{\rho}\tilde{E}, \bar{\rho}\tilde{Y}_k\}$ where ρ, u_j, E and Y_k are the density, jth component of velocity, specific total energy and kth species mass fraction, respectively. These equations are given in Calhoon (1996) and Fureby and Möller (1995) and are not repeated here for brevity.

The effect of the small unresolved scales appears as additional unknown terms in the resolved field equations. In the momentum equation, two additional terms arise which are the SGS stress tensor τ_{ij}^{sgs}, given by,

$$\tau_{ij}^{sgs} = \bar{\rho}(\widetilde{u_i u_j} - \tilde{u}_i\tilde{u}_j) \qquad (2)$$

and the filtered viscous stress tensor $\overline{\tau}_{ij}$,

$$\overline{\tau}_{ij} = \overline{\mu(\frac{\partial u_i}{\partial x_j} + \frac{\partial u_j}{\partial x_i} - \frac{2}{3}\delta_{ij}\frac{\partial u_l}{\partial x_l})} \qquad (3)$$

where μ is the viscosity and δ_{ij} is the Kronecker delta tensor. The unclosed terms in the filtered energy equation are the SGS total enthalpy flux H_j^{sgs}, the filtered heat flux $\bar{q}_j$ and the SGS viscous work term σ_j^{sgs} given by,

$$\begin{aligned} H_j^{sgs} &= \bar{\rho}(\widetilde{(h + \frac{u_k u_k}{2})u_j} - (\tilde{h} + \frac{\tilde{u}_k\tilde{u}_k}{2})\tilde{u}_j) \qquad (4)\\ &= \bar{\rho}(\widetilde{Hu_j} - \tilde{H}\tilde{u}_j) \end{aligned}$$

$$\overline{q}_j = \overline{-\lambda\frac{\partial T}{\partial x_j}} + \overline{\rho\sum_{k=1}^{K} h_k Y_k U_{k,j}} \qquad (5)$$

$$\sigma_j^{sgs} = \bar{\rho}(\widetilde{u_i\tau_{ji}} - \tilde{u}_i\overline{\tau}_{ji}) \qquad (6)$$

where h, T and λ are the mixture enthalpy, temperature and thermal conductivity, respectively. h_k and $U_{k,j}$ are the kth species enthalpy and jth component of diffusion velocity, respectively.

Unclosed terms in the species conservation equations are the convective species fluxes due to subgrid fluctuations $\Phi_{k,j}^{sgs}$, given by,

$$\Phi_{k,j}^{sgs} = \bar{\rho}(\widetilde{Y_k u_j} - \tilde{Y}_k\tilde{u}_j) \qquad (7)$$

the species diffusive fluxes $\theta_{k,j}^{sgs}$,

$$\theta_{k,j}^{sgs} = \bar{\rho}(\widetilde{Y_k U_{k,j}} - \tilde{Y}_k\tilde{U}_{k,j}) \qquad (8)$$

and the filtered species production rate $\overline{\dot{w}}_k$, where $\dot{w}_k$ is typically expressed in Arrhenius form (Williams, 1985).

In addition to the conservation equations, the equation of state for a multi-component fluid must also be filtered. The unfiltered state equation is given by $p = \rho R^\circ T \sum_{k=1}^{K} Y_k/W_k$ where K is the total number of species, R° is the universal gas constant and W_k is the kth species molecular weight. Applying the filtering to this equation results in,

$$\bar{p} = \bar{\rho} R^\circ \tilde{T} \sum_{k=1}^{K} \frac{\tilde{Y}_k}{W_k} + \bar{\rho} R^\circ \sum_{k=1}^{K} \frac{T_k^{sgs}}{W_k} \tag{9}$$

where T_k^{sgs} contains temperature-species correlations and is given by,

$$T_k^{sgs} = \widetilde{TY}_k - \tilde{T}\tilde{Y}_k \tag{10}$$

The filtering must also be applied to the caloric equation of state for mixture internal energy e, $e = h - p/\rho$, with the mixture enthalpy h specified in terms of the species heat of formation Δh_k° and specific heats $c_{p,k}$ (Williams, 1985). Specifying the $c_{p,k}$'s in terms of polynomial approximations (Kee *et al.*, 1989), this equation becomes (Calhoon, 1996),

$$\begin{aligned} \tilde{e} \;=\; & \sum_{k=1}^{K} \tilde{Y}_k(\Delta h_k^\circ - g_k(T^\circ)) \\ & + \sum_{k=1}^{K} \tilde{Y}_k(g_k(\tilde{T}) - \frac{R^\circ}{W_k}\tilde{T}) \\ & + \sum_{k=1}^{K} (a_{k,1} - \frac{R^\circ}{W_k}) T_k^{sgs} + T_k^{sgs,n} \end{aligned} \tag{11}$$

where,

$$g_k(T) = \sum_{n=1}^{N} a_{k,n} \frac{T^n}{n} \tag{12}$$

and $T_k^{sgs,n}$ contains higher order temperature-species correlations of the form,

$$T_k^{sgs,n} = \sum_{k=1}^{K} \sum_{n=2}^{N} a_{k,n} \frac{(\widetilde{Y_k T^n} - \tilde{Y}_k \tilde{T}^n)}{n} \tag{13}$$

$a_{k,n}$ is the nth coefficient of the Nth order polynomial approximating $c_{p,k}$.

To solve the LES conservation equations, these unknown terms must be closed with appropriate subgrid models. The SGS stress tensor τ_{ij}^{sgs} and the enthalpy flux term H_j^{sgs} are not unique to reacting flows and also appear in the compressible nonreacting LES equations. As a result, standard models for these terms may be adopted. In this study, τ_{ij}^{sgs} and H_j^{sgs} are modeled using the compressible extension (Nelson, 1995) of the *Localized Dynamic k-Equation Subgrid-Scale* (LDKSGS) model of Kim and Menon (1995). This model requires the solution of an additional modeled equation for the subgrid turbulent kinetic energy defined as $k^{sgs} = (\widetilde{u_l u_l} - \tilde{u}_l \tilde{u}_l)/2$. The subgrid terms related to diffusive processes (i.e. $\theta_{k,j}^{sgs}$, σ_j^{sgs} and the unresolved parts of $\bar{\tau}_{ij}$ and $\bar{q}_j$) are generally neglected in both reacting and nonreacting simulations. This is true even for high temperature flames where molecular properties may change rapidly (e.g. Fureby and Möller, 1995). This approach is also adopted here. However, this issue should be investigated in future studies.

The principle difficulty in reacting LES simulations is the proper modeling of the combustion related terms involving the temperature and species which are: 1) the convective species fluxes $\Phi_{k,j}^{sgs}$ due to subgrid fluctuations, 2) the temperature-species correlations T_k^{sgs} and $T_k^{sgs,n}$ and 3) the filtered species mass production rate $\overline{\dot{w}}_k$. The LEM model applied as a subgrid model is used in the present study to address these unclosed combustion related terms.

The next section gives a brief description of the LEM model before its implementation into LES is described.

3 LINEAR-EDDY MODEL

The LEM model has been described extensively by Kerstein (1988, 1989, 1990, 1991 1992) and is, therefore, only briefly discussed here. This model is designed to separately treat two fundamental physical processes which describe the evolution of chemical species in turbulent flames. These two processes are molecular diffusion and turbulent convective stirring. Molecular diffusion is treated within the model deterministically by the numerical solution of the species and temperature diffusion equations (Calhoon *et al.*, 1995) which include the effects of chemical reactions. Turbulent stirring, however, is modeled stochastically by a series of instantaneous rearrangement events of the species and temperature fields. These rearrangement events correspond to mixing induced by turbulent eddies. The length scale and frequency of these eddies are determined from relationships derived by Kerstein (1992). These relationships were derived by equating the diffusivity of a random walk of a fluid particle under the influence of the rearrangement events with the scaling of turbulent diffusivity.

The strategy employed within the LEM model is to resolve all relevant fluid mechanical length scales of the flow, as in direct numerical simulations. As a result, the reaction rate terms in the species and temperature equations appear in closed form and do not require additional modeling. Resolving all the length scales of the flow, however, will in general be computationally intractable in the foreseeable future. As a result, the LEM model is implemented in only one spatial dimension to keep the simulations affordable.

One underlying assumption in the model is constant pressure. As a result, the LEM fluid elements will necessarily expand with temperature increase. This expansion will cause a decrease in the local scalar gradients in the vicinity of the flame and thereby a reduction in molecular diffusion. Algorithms for the implementation of volumetric expansion within the LEM model have been described

by Kerstein (1991) and Goldin and Menon (1996). The procedure employed in this study is similar to that of Goldin and Menon (1996) and is described in detail in Calhoon (1996).

Inputs for the LEM model are the integral length scale L_{LEM}, the model Reynolds number Re_{LEM} (defined below), pressure, the species molecular diffusivities, thermal conductivity λ, species specific heats $c_{p,k}$ and the reaction rate constants. With specification of appropriate initial and boundary conditions, the species and temperature fields evolving in homogeneous, stationary turbulence can be determined (see McMurtry *et al.* (1993) for a description of the nonreacting mixing case). These fields can be used to directly compute subgrid temperature and species correlations needed for the LES simulation. One striking advantage of this approach over other formulations is the explicit inclusion of Reynolds number and molecular diffusivities in the model.

4 LEM SUBGRID MODEL

The LEM model may be used as a subgrid model for the small unresolved scales of the flow while the larger scales are calculated directly from the LES equations of motion. This approach requires the prescription of a method to couple the 1-D LEM model with the multi-dimensional LES resolved field equations. One approach to accomplish this task is called *LEM pdf calculation* (LEMC) approach. The LEMC method was first developed by Menon *et al.* (1993b) in the context of premixed flames. It has also been applied to describe diffusion flame structure by McMurtry *et al.* (1992) and Calhoon and Menon (1996). The LEMC method has been described in detail by Menon *et al.* (1993b), McMurtry *et al.* (1992), Calhoon (1996), Calhoon and Menon (1996) and Menon and Calhoon (1996). As a result, the method is only outlined here for brevity.

The strategy adopted in the LEMC approach is to explicitly implement a 1-D LEM spatial domain within the subgrid of each LES grid cell. Given the processes that effect the LEM subgrid fluid elements, the evolution of the subgrid species and temperature fields and their associated subgrid joint pdf is then calculated directly during the LES simulation.

The LEMC procedure seeks to model all the processes, both large and small scale, which influence the evolution of the subgrid Y_k fields. As a result, the filtered species $\tilde{Y}_k$ may be calculated directly by filtering the subgrid Y_k fields. This obviates the need to solve the LES filtered equations for $\tilde{Y}_k$. Consequently, use of conventional models for $\Phi^{sgs}_{k,j}$ employing the gradient diffusion assumption is completely avoided. Within the LEMC approach, modeling of the small scale processes is accomplished using the LEM model. The Y_k fields are also influenced by large scale convection. This process is modeled by employing a modified version (Calhoon, 1996) of the "splicing" algorithm developed by Menon *et al.* (1993b) which convects subgrid fluid elements from one LES cell to another. One advantageous property of this convection algorithm is that it treats species convection in a manner similar to Lagrangian schemes. That is, convection is independent of the magnitude or gradient of the species which are transported and depends only on the velocity field.

The processes effecting the evolution of the subgrid scalar fields are 1) molecular diffusion, 2) chemical reaction, 3) subgrid turbulent stirring, 4) volumetric expansion due to heat release and 5) large scale convection. These processes can be characterized by the time scales Δt_{diff}, Δt_{chem}, Δt_{stir}, Δt_{vol} and Δt_{conv}, respectively. Given these time scales, the temporal evolution of the subgrid scalar fields is represented within the LEMC procedure as follows. Given the initial subgrid scalar fields in each LES cell, the processes of molecular diffusion, chemical reaction, turbulent stirring, volumetric expansion and large scale convection are implemented as discrete events occurring in time. The epochs of these events are determined by the respective time scales of each process. This type of discrete implementation is similar to the fractional step method used to solve differential equations.

As the subgrid T and Y_k fields evolve under the action of these processes, the resolved scale LES equations for $\{\bar{\rho}, \bar{\rho}\tilde{u}_j, \bar{\rho}\tilde{E}\}$ are also solved concurrently on the acoustic time scale Δt_{LES}. The resolved scales may be coupled to the subgrid scalar fields and subgrid heat release as described by Menon *et al.* (1993a) or by a modified scheme described by Calhoon (1996). In this study, the coupling approach of Calhoon (1996) is employed and is outlined below.

4.1 COUPLING WITH THE RESOLVED SCALES

The subgrid and resolved scale fields are coupled to one another in the following ways. First, the subgrid fields are influenced by the resolved scales through the inputs to the LEM model and through the splicing algorithm. The inputs to the model are the subgrid length scale L_{LEM}, the model Reynolds number Re_{LEM}, pressure, the fluid transport properties, chemical reaction rate constants and the initial subgrid scalar distributions. L_{LEM} is specified equal to the LES characteristic filter size Δ_{LES}. Re_{LEM} is specified in terms of k^{sgs} as $\mathrm{Re}_{LEM} = \sqrt{k^{sgs}} L_{LEM}/\nu$ with ν being the kinematic viscosity based on the resolved field. The initial conditions for the subgrid fields are determined from the splicing or large scale convection events occurring on the time scale Δt_{conv}. Each splicing event transfers subgrid fluid elements from one LES cell to another generating new Y_k and T distributions which then evolve as prescribed by the LEM model.

A second subgrid-resolved scale coupling mechanism is the way in which the revolved fields are influenced by the subgrid through the subgrid closure terms and through subgrid heat release. The subgrid terms required to close

LES equations are the temperature-species correlations T_k^{sgs} and $T_k^{sgs,n}$. These correlations appear in the filtered state equations (9) and (11) and may be calculated from the subgrid fields. The filtered species $\tilde{Y}_k$ is also required in the state equations and in the filtered heat flux term in the resolved scale energy equation. $\tilde{Y}_k$ may also be calculated from the subgrid.

Before describing how the subgrid fields may be used to calculate resolved scale variables, the following notation is introduced in order to clarify the discussion in this section. Let $B|_{LEM}$ represent the value of some variable B calculated from the *subgrid* LEM fields. With this notation, for example, $\tilde{Y}_k\Big|_{LEM}$ represents the filtered species mass fraction calculated by directly filtering the subgrid LEM Y_k field within an LES grid cell. $\tilde{Y}_k$, on the other hand, represents the LES resolved scale value of species mass fraction in the LES equations. The subgrid filtering (via equation (1)) used to obtain $\tilde{Y}_k\Big|_{LEM}$ is only performed within each LES cell to be consistent with the form of the *box* spatial filter function used in this study.

One approach to calculate $\tilde{Y}_k$, for example, from the subgrid fields is to simply specify $\tilde{Y}_k = \tilde{Y}_k\Big|_{LEM}$. However, the $\tilde{Y}_k\Big|_{LEM}$ field will not be resolved across LES cell boundaries. This is due to the fact that the subgrid molecular diffusion and stirring processes are not implemented across LES cell boundaries, by assumption (Menon *et al.*, 1993b; Calhoon, 1996). These subgrid processes are confined to only act upon subgrid fluid elements within individual LES cells. Specifying $\tilde{Y}_k = \tilde{Y}_k\Big|_{LEM}$ will be unacceptable because the LES equations, by definition, require the filtered variables to be resolved from one LES cell to another. To alleviate this difficulty, $\tilde{Y}_k$ in LES equations is specified as,

$$\tilde{Y}_k = \left\langle \tilde{Y}_k\Big|_{LEM} \right\rangle \tag{14}$$

where the brackets $\langle\ \rangle$ denotes filtering using equation (1) with characteristic filter width $\hat{\Delta}_{LES} = 2\Delta_{LES}$. This will eliminate the unresolved fluctuations in $\tilde{Y}_k\Big|_{LEM}$ across LES cell boundaries and will yield a well resolved $\tilde{Y}_k$ field for the LES equations. The subgrid temperature-species correlations T_k^{sgs} and $T_k^{sgs,n}$ may similarly be approximated by,

$$T_k^{sgs} = \left\langle T_k^{sgs}|_{LEM} \right\rangle \tag{15}$$

$$T_k^{sgs,n} = \left\langle T_k^{sgs,n}|_{LEM} \right\rangle \tag{16}$$

The expressions given by equations (14)–(16) do not change the values of the subgrid temperature and species fields. These expressions only prescribe the way in which the LES filtered equations "see" or relate to the subgrid. The resolved scale values of $\tilde{Y}_k$, T_k^{sgs} and $T_k^{sgs,n}$ may be viewed as approximations of subgrid correlations based on the unfiltered subgrid distributions. Other statistical quantities involving $\tilde{Y}_k$, for example, should, therefore, be calculated directly from the subgrid and not from values of $\tilde{Y}_k$ obtained using equation (14).

The filtering described by equations (14)–(16) is needed as a result of the assumptions made within the formulation. This filtering is not based on physical reasoning but on the need to remove unresolved scales across LES cell boundaries. *Pdf evolution equation* methods (Pope, 1985; Pope, 1990) face a similar difficulty and resolve the situation by, for example, smoothing the cell averaged fields using *smoothing cubic splines* (Pope, 1985). A similar technique could be used here in place of the filtering given in equations (14)–(16). However, the filtering is used here as a matter of convenience because the filtering function $\langle\ \rangle$ is already employed in the dynamic LDKSGS model used to close the resolved scale momentum and energy equations. This is an issue for further investigation.

Given values of $\tilde{Y}_k$, T_k^{sgs} and $T_k^{sgs,n}$ from equations (14)–(16), subgrid heat release may then be coupled with the resolved scales through the state equations. The only remaining issue is to define how the resolved temperature $\tilde{T}$ is to be calculated. This may be done by two different approaches. For reference purposes, these approaches are denoted *Coupling Method 1* and *Coupling Method 2* and are described below.

Within Coupling Method 1 the resolved temperature field $\tilde{T}$ is determined from equation (11) given $\tilde{Y}_k$, T_k^{sgs} and $T_k^{sgs,n}$ (calculated from the subgrid) and $\tilde{e}$ calculated from the resolved scale equation for $\bar{\rho}\tilde{E}$. A second value of $\tilde{T}$ can also be calculated directly from the subgrid as,

$$\tilde{T} = \left\langle \tilde{T}\Big|_{LEM} \right\rangle \tag{17}$$

These two predictions are then compared. Significant disagreement in these predictions imply two possibilities. The first possibility is that the assumptions used in the LEMC procedure have been violated. These assumptions are 1) the effect of viscous work on the subgrid is negligible, 2) constant subgrid pressure is assumed to derive the subgrid temperature equation (Calhoon *et al.*, 1995; Calhoon, 1996) and 3) thermal conduction is negligible across LES cell boundaries.

The second possibility implied by disagreement in the two predictions for $\tilde{T}$ within Coupling Method 1 is that the subgrid model used for the total enthalpy flux term H_j^{sgs} (equation (4)) is in error. As previously mentioned, this term appears in the filtered energy equation and is modeled using the gradient diffusion assumption as,

$$H_j^{sgs} = -\bar{\rho}\nu_H \frac{\partial \tilde{H}}{\partial x_j} \tag{18}$$

where ν_H is determined dynamically from the LDKSGS model (Calhoon, 1996). An improper estimation of H_j^{sgs} using this model will degrade the prediction of $\tilde{e}$ from the filtered energy equation, resulting in errors in the calculation of $\tilde{T}$ from equation (11). Expanding equation (4)

reveals that H_j^{sgs} contains velocity-temperature-species correlations. The influence of these correlations may not be well represented by the model given in equation (18).

Good agreement of the two predictions for $\tilde{T}$ within Coupling Method 1, on the other hand, implies the validity of the LEMC assumptions and the appropriateness of the modeled total enthalpy flux. This coupling approach is advantageous because it provides a measure of the validity of the subgrid modeling.

Within Coupling Method 2, the resolved temperature field $\tilde{T}$ is calculated directly from the subgrid as given by equation (17). This approach obviates the need to solve the filtered energy equation for $\bar{\rho}\tilde{E}$. This coupling method has the advantage that it reduces the computational requirements by reducing the number of equations which must be solved. Also, this method eliminates the need to model H_j^{sgs}, avoiding the uncertainties associated with the eddy viscosity model in equation (18). However, this method implies that the assumptions in the subgrid model (noted earlier) are being implicitly satisfied.

An additional coupling concern may arise when reduced chemical mechanisms are used to approximate the subgrid chemistry. Many reduced mechanism assume constant pressure. In this case, the input pressure to the LEM model is specified as the reduced mechanism assumed pressure. The two coupling methods described above may be applied to this case but with a small modification. These coupling methods must be modified to include a comparison of LES filtered pressure $\bar{p}$ calculated from equation (9) with the reduced mechanism assumed pressure. Significant disagreement in these values for pressure again indicates a breakdown of the underlying assumptions and the subgrid modeling.

4.2 Model calibration

The LEMC subgrid model has previously been applied to reacting mixing layers without heat release effects in Calhoon and Menon (1996). In that study, the subgrid model was calibrated using the experimental data of Mungal and Dimotakis (1984) for the integral of the layer normalized product at different Reynolds numbers. This calibration yielded good simulated results for both infinite and finite rate chemistry cases(Calhoon and Menon, 1996). The calibration procedure is described in detail by Calhoon(1996) and Calhoon and Menon (1996) and is not included here. With no logical basis for change, the value of calibration coefficient obtained by Calhoon and Menon (1996) is retained for the heat release cases presented in this study.

5 Numerical formulation

The modeled LES equations for $\{\bar{\rho}, \bar{\rho}\tilde{u}_j, \bar{\rho}\tilde{E}\}$ are solved numerically in finite volume form. The inviscid cell face fluxes are approximated using the AUSM flux split scheme (Liou and Steffen, 1993) extended to fifth order using the MUSCL approach. The fifth order interpolation is upwind-biased with a stencil given by Hariharan and Sankar (1994). This stencil is also modified in the vicinity of steep gradients using the *Adaptive Essentially Non-Oscillatory* scheme of Hariharan (1995). The viscous stresses and heat flux terms are evaluated with the fourth order scheme of Bayliss *et al.* (1985). All other spatial derivatives in the LES equations are approximated to fourth order using central differences. Time advancement is accomplished using a second order Runga-Kutta scheme. The LES time step (Δt_{LES}) is fixed in all simulations and corresponds to a CFL number of $\leq .3$, which is below the stability requirement.

The subgrid LEM diffusion equations are discretized using a second order central difference scheme on an equally spaced grid. This discretization was validated by comparison with an exact solution of the diffusion equation. It should also be noted that a test conducted using a sixth order compact scheme showed only a small improvement over the second order central difference scheme. Consequently, the second order scheme was adopted due to its simplicity.

The grid spacing in the subgrid is specified as $\Delta s = L_{LEM}/N_{LEM}$ where N_{LEM} is the number of subgrid fluid elements and s is the subgrid spatial coordinate. The subgrid equations are time advanced using the backward Euler scheme with the time scales Δt_{diff} and Δt_{chem} specified from stability considerations (Calhoon, 1996). The time scale Δt_{stir} of the LEM model is specified following Menon *et al.* (1993b) with $L_{LEM} = \Delta_{LES}$.

The final small scale process to be described is subgrid volume expansion. A detailed description of this process and its implementation is given by Calhoon (1996) and is only outlined here. Volume expansion in the subgrid is applied on the time scale Δt_{vol} which is in general set equal to the molecular diffusion time scale Δt_{diff}. After solving the subgrid diffusion equations, the resulting subgrid fields are expanded based on local temperature changes since the subgrid pressure is assumed constant. Each subgrid fluid element will, in general, expand different amounts resulting in a nonuniformly spaced subgrid. The resulting subgrid distributions are then re-gridded back onto a uniform grid with spacing Δs equal to the spacing of the of original unexpanded grid.

Once the subgrid has been expanded and re-gridded, the *total* number of expanded subgrid fluid elements will be larger than N_{LEM} for the original grid. There are two approaches to handling this situation. Within the first approach, the LEMC model is formulated to allow N_{LEM} to vary throughout the LES domain. In this case, dilation at the resolved scales induced by the subgrid-resolved scale coupling will cause these additional subgrid elements to be convected into neighboring LES cells and eventually out of the computational domain. Therefore, the number of subgrid fluid elements within each LES cell will, on average, remain constant.

The second approach for handling the extra subgrid

elements introduced by volume expansion is to randomly truncate the expanded subgrid domain to maintain constant N_{LEM}. This approach has been used by Menon *et al.* (1993a) and Menon *et al.* (1993b) in the context of premixed flames. This truncation obviously introduces a mass error. However, since the truncation is random, this error will not build up and will, on average, be zero. The remaining subgrid fields will also be a representative statistical sample of the original fields. If the heat release level in a simulation is high, however, the instantaneous error may become intolerable. As a result, this approach should only be applied to simulations with low to moderate heat release levels.

Allowing N_{LEM} to vary in the LES domain has the advantage that arbitrarily high levels of heat release may be considered without introducing mass errors. However, the disadvantage of this approach is the additional complexity of the algorithm. Truncating the subgrid fields has the disadvantage of introducing instantaneous mass errors but has the advantage of computational simplicity and speed. For simulations with low to moderate heat release levels, the truncation approach provides an acceptable compromise between accuracy and complexity. This truncation approach is adopted in this study. Therefore, the simulations presented here are restricted to moderate heat release levels. Verification of this modeling approach is accomplished through direct comparison with experimental results.

The final time scale to be specified within the LEMC approach is Δt_{conv} of the splicing algorithm. This is a velocity time scale and is taken as,

$$\Delta t_{conv} = \frac{\prod_i \Delta x_i}{|\varepsilon_{i,j,k}|\, \tilde{u}_i \Delta x_j \Delta x_k} \tag{19}$$

where Δx_i is the LES grid cell width in the ith coordinate direction and $\varepsilon_{i,j,k}$ is the Levi-Civita tensor.

Validation tests of the individual components of the model have been carried out and are described by Calhoon (1996). Additional *quantitative* and *qualitative* validation of the complete model has also be demonstrated by Calhoon and Menon (1996) for negligible heat release reacting mixing layers.

6 Reacting Mixing Layer with Heat Release

This section describes the application of the LEMC subgrid approach to the LES modeling of mixing and reaction in high Reynolds number mixing layers with heat release. The combined modeling approach will be denoted the LES-LEMC method. Reacting mixing layers have been extensively studied experimentally for a wide range of conditions (see Dimotakis, 1989, for a recent review). The results of these experiments provide an opportunity to demonstrate the capabilities of the LES-LEMC approach.

In this study, the simulations are restricted to temporally evolving layers in only two spatial dimensions. Experiments have shown the early stages of development of many mixing layers to be dominated by large, 2-D, coherent structures (Dimotakis, 1989; Roshko, 1976). These structures may also persist to considerable downstream distances. However, 3-D effects are known to play a crucial role in turbulent mixing (Park *et al.*, 1994), especially for mixing layers with Reynolds numbers above the mixing transition (Breidenthal, 1981). The mixing transition is characterized by a large increase in the 3-D motions in the flow and a large increase in turbulent mixing. These 3-D motions, however, are confined to only the small scales during the early stages of mixing layer development (Breidenthal, 1981). Further downstream, 3-D motions may become a dominant effect. It has also been observed for mixing layers, both experimentally (Ganji and Sawyer, 1980) and computationally (McMurtry *et al.*, 1989), that heat release causes a significant reduction in 3-D motions and that the large 2-D coherent structures may exist even at high levels of heat release.

Within the 2-D application of the LES-LEMC approach to model reacting mixing layers, the development of the large scale coherent structures in the flow are modeled by the LES resolved field equations. The 3-D small scale mixing effects are modeled by the LEMC subgrid approach which relies on the LEM mixing model. The LEM model, although only a 1-D approximation, has been shown to capture 3-D mixing effects in homogeneous, stationary turbulence (McMurtry *et al.*, 1993). This 2-D large scale/3-D small scale formulation of the LES-LEMC method may, therefore, provide a realistic representation of the early stages of development of physical mixing layers. This formulation also makes it possible to predict the post mixing transition behavior of high Reynolds number layers. This is unattainable in a purely 2-D simulation because there is no mechanism for 3-D small scale mixing, as recently demonstrated by Park *et al.* (1994).

The simulations presented here seek to model mixing layers with dilute reactant species. Within this configuration, several simplifying assumptions are possible. For example, Fickian diffusion with equal diffusivities for all species maybe assumed. With this assumption the mixing process can be completely described in terms of the Shvab-Zeldovich mixture fraction ξ (Williams, 1985). ξ is the normalized mass fraction of an atomic species originating in the fuel stream. ξ is, therefore, one in the fuel stream and zero in the oxidizer stream. The LEM subgrid diffusion equation for ξ is given by,

$$\frac{\partial \xi}{\partial t} = \frac{1}{\rho}\frac{\partial}{\partial s}\left(\rho D \frac{\partial \xi}{\partial s}\right) \tag{20}$$

where the diffusion coefficient is taken as $D = \nu/Sc$. The Schmidt number Sc for all simulations is set equal to .7 which is characteristic of gases. The unreacted species in the subgrid are linearly related to ξ and can be found given their values in the fuel and oxidizer streams.

The reaction chemistry in the layer is assumed to be governed by the elementary irreversible reaction $F + O \rightarrow P$. This reaction is also assumed to proceed at an infinite rate. Product formation may then be calculated given ξ by assuming complete conversion of all reactant species.

The subgrid pressure is also assumed constant and equal to a reference value of 1 *atm*. The simulations are also carried out at low Mach number. In addition, the Lewis number, $Le = \lambda/\rho c_p D$, is also assumed to be equal to one. With these assumptions, the subgrid energy equation reduces to the same form as equation (20). The subgrid enthalpy may then be expressed as $h = \xi h_1 + (1-\xi)h_2$ (Williams, 1985) where h_1 and h_2 are the freestream values of h on the upper and lower sides of the layer, respectively. The subgrid temperature is then directly related to ξ.

Two types of simulations are described in this section. In the first type, the reactant species F and O are diluted in inert fluids D_1^* and D_2^*, respectively, as in the experiments of Hermanson and Dimotakis (1989). The molecular weights of species F and O are taken equal to the molecular weights of hydrogen and fluorine, respectively. The inert fluid D_1^* is taken as a mixture of nitrogen and argon while fluid D_2^* is taken as a mixture of nitrogen and helium. The composite molecular weights of D_1^* and D_2^* are set so that the freestream fuel and oxidizer mixtures have equal densities and specific heats at constant pressure, assuming equal freestream temperatures. In the second type of simulation the species F and O are not diluted and freestream densities and specific heats are not the same. In these simulations the molecular weights of F and O are also set equal to the molecular weights of hydrogen and fluorine, respectively.

The species specific heats at constant pressure $c_{p,k}$ are assumed to be constant in all simulations. The $c_{p,k}$'s are evaluated from general temperature dependent expressions evaluated at the freestream temperatures. The mixture viscosity, however, is allowed to vary with temperature as specified by,

$$\mu = \frac{C_{\mu,1} T^{3/2}}{C_{\mu,2} + T} \tag{21}$$

with $C_{\mu,2} = 110.4$ and $C_{\mu,1} = 0.00014$.

The computational domain for the simulations is a $H \times (H/2 + \Delta H)$ box where $H = 2\pi$. The grid is equally spaced in the streamwise x_1 and transverse x_2 directions on the range $-H/2 \leq x_1 \leq H/2$ and $-H/4 \leq x_2 \leq H/4$ with $\Delta x_1 = \Delta x_2 = H/N_{LES}$. For $H/4 \leq |x_2| \leq (H/2 + \Delta H)/2$, the grid is stretched and the AUSM flux split scheme is reduced from fifth to third order. This grid stretching and order reduction of the scheme are used in order to damp acoustic waves moving toward the upper and lower boundaries. N_{LES} for these simulations is 128 and the stretched portion of the grid contains 20 additional points on both the top and bottom. A stretching factor of 1.2 is used to distribute these points.

Periodic boundary conditions are applied in the streamwise direction x_1. On the upper and lower boundaries, the nonreflecting boundary conditions of Baum *et al.* (1994) extended to include the species heat of formation (Calhoon, 1996) are applied in 1-D normal to the boundary at $x_2 = \pm(H + \Delta H)/2$. The nonreflecting conditions are employed to allow outward moving pressure waves to leave the domain and inhibit boundary reflections from influencing the layer development. Also, these boundary conditions allow the heat release simulations to evolve at constant mean pressure.

The subgrid LEM resolution N_{LEM} is chosen based on the criteria that the smallest length scales of the flow be resolved. With $Sc = 0.7$, the smallest scale is the Kolmogorov scale. A subgrid resolution of $N_{LEM} = 400$ is found to adequately resolve this scale. In fact, increasing heat release improves the resolution because temperature increases reduce the subgrid Reynolds number, increasing the size of the Kolmogorov length scale.

The resolved velocity field $\tilde{u}_j$ is initialized as a mean field plus a perturbation. The mean velocity is specified by,

$$\begin{aligned} \langle u_1 \rangle_{mean} &= \frac{U_o}{2} \tanh(x_2/\alpha) \\ \langle u_2 \rangle_{mean} &= 0 \end{aligned} \tag{22}$$

where $\langle B \rangle_{mean}$ denotes the mean value of B averaged in the periodic direction. U_o is the velocity difference across the layer and α is a constant related to the initial vorticity thickness $\delta_{\omega,o}$. The vorticity thickness is defined by,

$$\delta_\omega = U_o \left[\frac{\partial \langle u_1 \rangle_{mean}}{\partial x_2} \right]^{-1}_{\max} \tag{23}$$

Applying this definition to $\langle u_1 \rangle_{mean}$ in equation (22) yields $\delta_{\omega,o} = 2\alpha$. In all the simulations presented in this study $\alpha = .1496$. From linear stability analysis (Michalke, 1964), this value of α causes the third spatial mode of the layer to be the most unstable, assuming constant density.

The perturbation velocity added to $\langle u_j \rangle_{mean}$ is specified in a manner similar to Riley and Metcalfe (1980). The perturbation is taken as an isotropic velocity field with an energy spectrum which decays as k^{-2} where k is the magnitude of the spectral wave number vector k_j. This velocity field is then modified by a form function which preserves the divergence free property and gives a streamwise velocity fluctuation $\langle u_1 \rangle_{rms}$ of the form (Riley and Metcalfe,1980),

$$\frac{\langle u_1 \rangle_{rms}}{U_o} = .18 \exp(-.147(2x_2/\delta_{1/2})^2) \tag{24}$$

where $\delta_{1/2}$ is the velocity half width of $\langle u_1 \rangle_{mean}$.

U_o for all simulations is set to 71 $m/\sec$. This corresponds to a convective Mach number M_c of ≈ 0.1 for

most of the simulations, assuming a reference temperature T_o of 300 K on both sides of the layer. The convective Mach number is defined by $M_c = U_o/(a_1 + a_2)$ where a_1 and a_2 are the freestream speeds of sound on the upper and lower sides of the layer, respectively. This value of M_c is low enough that compressibility effects are small. The resolved pressure $\bar{p}$ is initialized constant in the domain and equal to 1 atm. The initial resolved density $\tilde{\rho}$ and temperature $\tilde{T}$ are set equal to their adiabatic flame values given $\tilde{\xi}$ (described below).

The subgrid kinetic energy is initialized following Kim and Menon (1995) using $k^{sgs} \cong C_K k^{res}$ with $C_K = 0.45$. k^{res} is the turbulent kinetic energy on the length scale $2\Delta_{LES}$ and is calculated directly from the initial velocity field (Calhoon, 1996). k^{res} is estimated assuming constant density equal to that of air at 1 atm and $300K$. This choice is made so that all simulations have the same initialization for k^{sgs}.

The LEM subgrid mixture fraction is initialized as constant in each LES cell and equal to a filtered value specified by,

$$\tilde{\xi} = \frac{1}{2}(1 + \tanh(x_2/\alpha)) \tag{25}$$

For the mixing layer simulations considered in this section, the temperature-species correlations T_k^{sgs} given by equation (10) may be large. These correlations appear in the filtered state equations as described earlier. Assuming the species to have constant specific heats, equation (11) may be rewritten as,

$$\begin{aligned} \tilde{e} &= \sum_{k=1}^{K} \tilde{Y}_k \left(\Delta h_k^\circ - c_{p,k} T^\circ\right) \\ &+ \sum_{k=1}^{K} \left(\tilde{Y}_k + T_k^{sgs}\right)\left(c_{p,k} + \frac{R^\circ}{W_k}\right) \end{aligned} \tag{26}$$

As discussed previously, T_k^{sgs} may be predicted using the LEMC subgrid model. However, for cases in which the density and the mixture specific heat c_p are the same on both sides of the layer, the contributions from this term are either zero or negligible. For these simulations, the mean molecular weight $W^m = \sum_{k=1}^{K} Y_k/W_k$ is a constant and it can then be shown that $\sum_{k=1}^{K} T_k^{sgs}/W_k = 0$. c_p is also approximately constant so that $\sum_{k=1}^{K} c_{p,k} T_k^{sgs} \approx 0$ as well. Contributions for T_k^{sgs} are, therefore, discarded in the simulation in which the properties are the same on both sides of the layer. For the case when the properties are different, however, the contributions from T_k^{sgs} may be large and must be included.

As described previously, subgrid volume expansion should in general be implemented on the time scale $\Delta t_{vol} = \Delta t_{diff}$. However, for the simulations presented in this paper, specifying Δt_{vol} equal to the acoustic time scale Δt_{LES} is found to adequately resolve this phenomena. In general, this modification may be employed to reduce the computational effort for cases in which the solution does not change appreciably when Δt_{vol} is relaxed to Δt_{LES}.

7 Results and Discussion

7.1 Heat Release with Constant Freestream Properties

The simulations described in this section assume equal freestream density and mixture specific heats. From this condition the freestream concentration of the diluent species may be calculated once the freestream concentrations of the reactant species F and O are specified. The reactant concentrations are specified in terms of the equivalence ratio ϕ, defined as the ratio of the low speed side reactant concentration to the high speed reactant concentration, divided by the stoichiometric low speed to high speed reactant concentration ratio. The high speed side is taken as the upper side of the layer carrying species F. For the elementary reaction considered here, the stoichiometric ratio of F to O is equal to one so that ϕ reduces to,

$$\phi = \frac{[O]_o}{[F]_o} \tag{27}$$

where the brackets $[B]_o$ denote the freestream concentration of reactant species B.

Two values of ϕ are considered in this section which are 1 and 1/4. For $\phi = 1$, the freestream concentrations of the species F and O are both specified as 6%. For $\phi = 1/4$, F and O concentrations are specified as 24% and 6%, respectively. The heat release for each value of ϕ is controlled by the product species heat of formation, Δh_P°, which is specified to achieve adiabatic flame temperature rises ΔT_{fl} of 0, 150, 300, 450, 600, 750 and 900 K for each value of ϕ.

The Reynolds number $\mathrm{Re}_{\omega,o}$ for the simulations is 13,100 and 11,500 for $\phi = 1$ and 1/4, respectively. $\mathrm{Re}_{\omega,o} = \rho_1 U_o \delta_{\omega,o}/\mu(T_o)$ where ρ_1 is the upper side freestream density, $\delta_{\omega,o}$ is the initial value of the vorticity thickness given by equation (23) and T_o is the freestream temperature which is 300 K on both sides of the layer. These values of $\mathrm{Re}_{\omega,o}$ are well past the mixing transition which is complete by $\mathrm{Re}_\omega \simeq 7000$ (Koochesfahani and Dimotakis, 1986).

As described in section 4.1, subgrid heat release must be coupled with the resolved scales. For the simulations described in this section, the subgrid temperature and species fields are coupled to the resolved scales using Coupling Method 1. Also, since the subgrid pressure is assumed to be equal to the reference pressure, this coupling scheme is modified as described in section 4.1. The effectiveness of the coupling will be discussed in a subsequent paragraph.

Figure 1 presents a plot of the growth of the energy in the third spatial mode of the layer for each level of heat release for $\phi = 1$. Recall from section 6 that the initial

thickness of the layer has been set so that the third mode is the most unstable, as determined from constant density analysis (Michalke, 1964). The modal energy $E_N(k_1)$ is calculated by integrating the spectral energy in the periodic direction across the layer as,

$$E_N(k_1) = \frac{1}{2}\int_{-(H+\Delta H)/2}^{+(H+\Delta H)/2} \left|\widehat{\rho^{1/2}\tilde{u}_1}\right|^2(k_1) + \left|\widehat{\rho^{1/2}\tilde{u}_2}\right|^2(k_1)\,dx_2 \quad (28)$$

where $\widehat{B}$ denotes the Fourier transform of variable B. $k_1 = 3$ in the figure. Time is nondimensionalized by $\delta_{\omega,o}/U_o$ and E_N is also nondimensionalized by U_o, $\delta_{\omega,o}$ and ρ_1. As seen in Figure 1, the third mode of the layer for all cases begins to grow shortly after the start of the simulation. After an initial development period, all cases show approximate linear growth before the energy in this mode peaks or saturates and begins to decline. Note that the growth rate in the linear region decreases with increasing heat release. The peak energy also decreases dramatically with increasing heat release. These two trends of the modal energy evolution have also been observed in the DNS simulations of Higuera and Moser (1994) for pre-transitional mixing layers carried out at $\mathrm{Re}_{\omega,o} = 2000$.

A plot of the modal energy for $\phi = 1/4$ (not shown here) also reveals the same trends observed in Figure 1. However, for the same adiabatic flame temperature rise, the $\phi = 1/4$ case is less affected by heat release than for $\phi = 1$. For $\phi = 1/4$, the growth rate suppression with heat increase is less than for $\phi = 1$ with the same ΔT_{fl} and the peak modal energies are higher. This suggests that less product is formed for values of ϕ not equal to 1. This is likely due to entrainment ratio effects as described Mungal and Dimotakis (1984) and Calhoon and Menon (1996) for negligible heat release reacting mixing layers. Product formation within the simulations will be discussed shortly.

The reduced growth rates seen in Figure 1 suggest that the overall growth of the layer is suppressed with heat release. The width of the layer may be characterized by the transverse scale δ_1 which is the length between the points at which the normalized mean temperature rise $(\langle T\rangle_{mean} - T_o)/\Delta T_{fl}$ is 1% of its maximum value. This length scale is commonly measured in reacting mixing layer experiments (Mungal and Dimotakis, 1984; Koochesfahani and Dimotakis, 1986; Hermanson and Dimotakis, 1989) and is plotted in Figure 2 for $\phi = 1$ and 1/4 and for different levels of heat release. δ_1 in this figure is calculated at a nondimensional time of $\tau = 11$ for all cases. Taking the data at a fixed time in the present temporal simulations is equivalent to collecting data at a fixed downstream location in an experiment. The time of $\tau = 11$ is in the approximate linear growth regime of Figure 1 and is prior to the third mode saturation time for all simulations. δ_1 in the figure is nondimensionalized by U_o and t_{conv} where t_{conv} is the simulation time or equivalent flight time starting from $\tau = 0$.

The length scale δ_1 in Figure 2 is plotted against the mean normalized density reduction $\Delta\rho/\rho_1$. This quantity was measured by Hermanson and Dimotakis (1989) for reacting mixing layers with varying amounts of heat release. Hermanson and Dimotakis carried out experiments for hydrogen-fluorine reaction in equal density mixing layers, similar to the present simulations. Following Hermanson and Dimotakis, the mean normalized density reduction is given by,

$$\Delta\rho/\rho_1 = (\rho^* - \rho_1)/\rho_1 \quad (29)$$

where ρ^* is expressed in terms of the mean temperature as,

$$\rho^* = \frac{\rho_1}{\delta_1}\int_{\eta_2}^{\eta_1} T_o/\langle T\rangle_{mean}\,d\eta \quad (30)$$

η_1 and η_2 are the x_2 locations at the edge of the layer where $(\langle T\rangle_{mean} - T_o)/\Delta T_{fl}$ is 1% of its maximum value.

From Figure 2 it can be seen that δ_1 decays approximately linearly with increasing heat release for both $\phi = 1$ and 1/4 after $\Delta\rho/\rho_1 \simeq 0.15$. This length scale is also seen to decay at the same rate for both values of equivalence ratio. Experimentally, Hermanson and Dimotakis (1989) also observed the linear decay of δ_1 with increasing heat release and found the rate to be independent of ϕ. Shear layer thinning with heat release has also been observed in the experiments of Ganji and Sawyer (1980) for premixed flames. However, Pitz and Daily (1983) did not observe any reduction of layer growth with heat release. Keller and Daily (1983), in fact, observed shear layer thickening with heat release in their experiments. Numerical simulations, on the other hand, have consistently reported shear layer thinning with heat addition (e.g. McMurtry *et al.*, 1989; Higuera and Moser, 1994; Soteriou and Ghoniem, 1994a). At this time, the variation among the experiments is unexplained. However, the discrepancies are likely due to differences in experimental setup and conditions (e.g. layer confinement, heat release level and flow configuration).

The thinning tend observed in Figure 2 is also apparent in the mean velocity profiles. Figure 3 presents a plot of the mean filtered streamwise velocity $\langle\tilde{u}_1\rangle_{mean}$ at $\tau = 11$ for $\phi = 1$ with heat release levels of $\Delta T_{fl} = 0$ and 900 K. The transverse coordinate has been nondimensionalized by $\delta_{\omega,o}$ which is the same for both cases. Note that the heat release case shows a steeper mean velocity gradient at the center of the layer, indicating layer thinning. This trend of the mean velocity is in agreement with experimental data of Hermanson and Dimotakis (1989) and with other numerical simulations including McMurtry *et al.* (1989). Also note the mean velocity overshoots at the edge of the layer for the heat release case. Overshoots in the mean velocity profile have also been observed numerically in the DNS simulations of McMurtry *et al.* (1989), Soteriou and Ghoniem (1994b) and others.

McMurtry *et al.* (1989) and Soteriou and Ghoniem (1994b) suggest that overshoots in the mean velocity are a result of vorticity generated by baroclinic torque ω_b. Baroclinic torque results from nonaligned pressure and density gradients and is given by,

$$\omega_b = \frac{1}{\rho}\varepsilon_{i,j,k}\frac{\partial \rho}{\partial x_k}\frac{\partial p}{\partial x_j} \tag{31}$$

where $\varepsilon_{i,j,k}$ is the Levi-Civita tensor. ω_b appears in the vorticity transport equation and may generate both positive and negative vorticity. By comparing results from cases with and without heat release, McMurtry *et al.* (1989) and Soteriou and Ghoniem (1994b) deduced that baroclinic torque was responsible for the velocity overshoots. This conclusion may be demonstrated more directly by conducting simulations in which the effects of baroclinic torque are removed. This may be done following Higuera and Moser (1994) by replacing the pressure gradient term $\partial p/\partial x_j$ in the momentum equations by $\rho \partial p/\partial x_j$. This modification sets ω_b to zero in the vorticity transport equation (derived by taking the curl of the momentum equations) without changing any other terms. Figure 3 includes a plot of the mean velocity for a case with $\phi = 1$ and $\Delta T_{fl} = 900\ K$ but with $\omega_b = 0$. For this case the velocity overshoot is not evident, in agreement with the conclusions of McMurtry *et al.* (1989) and Soteriou and Ghoniem (1994b). Also note that for $\omega_b = 0$, the layer becomes thicker than for the case with $\Delta T_{fl} = 0$. This is evident by the reduced centerline gradient when $\omega_b = 0$.

Figure 4 presents contour plots of the resolved vorticity at $\tau = 11$ for $\phi = 1$ with $\Delta T_{fl} = 0$ and $900\ K$. Velocity in this figure is moving to the right on the top of the layer and to the left on the bottom. It is evident from the figure that large scale coherent structures persist in the flow when heat release is present, as has been observed experimentally (Ganji and Sawyer, 1980; Keller and Daily, 1983; Pitz and Daily, 1983; Hermanson *et al.*, 1987). The structure of the vorticity field, however, is somewhat different between the two cases. First, the heat release case reveals reduced rotation rates of the large scale structures as is evident from the decreased vorticity magnitude in the vortex cores. This behavior can be attributed to the effect of volumetric expansion (McMurtry *et al.*, 1989). Expansion of a vortex due to heat release will result in a lower rotation rate and a decrease in vorticity magnitude in order to conserve angular momentum. Second, with heat release, the large scale structures are somewhat elliptical with the major axis oriented in the streamwise direction. Without heat release, the structures are more circular. This distortion of the large scale structures with heat release results in the reduced transverse width of the layer shown in Figure 2.

A third effect of heat release on the vorticity field can be observed from Figure 4. For the heat release case, there are regions with higher levels of positive vorticity around the large scale structures than for the case without heat. This is most evident on the transverse extremities of the large structures. These regions of increased positive vorticity correspond to locations of significant density gradients in the flow, indicating that they are a result of baroclinic torque. The density gradients can be seen in Figure 5 which presents contour plots of the filtered subgrid density and temperature fields for $\Delta T_{fl} = 900\ K$. For this case a small pressure gradient is present *across* the layer owing to gas expansion due to heat release. This gradient results in velocity outflow at the upper and lower boundaries of the computational domain. The transverse pressure gradient, as well as local pressure fluctuations, and the density gradients resulting from temperature variations seen in Figure 5 allow for the generation of vorticity due to baroclinic torque.

The differences seen in Figure 4 in the structure of the vorticity fields are a result of several effects. From the vorticity transport equation for low Mach number flows (McMurtry *et al.*, 1989), the vorticity field is altered by the effects of thermal expansion, baroclinic torque, viscous diffusion and vortex tube stretching. Vortex tube stretching is a 3-D effect and is zero at the large scales in the present simulations. This results from the 2-D assumption used in the resolve scale equations. At the small scales, the effect of the 3-D motions is accounted for within the LEMC subgrid model as described in section 6. Also recall from section 6 that the present simulations are applicable to the early time development of shear layers in which the 3-D motions are not dominant and are confined to only the small scales.

The effect of viscous diffusion on the development of the vorticity field is negligible at the large scales due to the high Reynolds number of the present simulations. The Reynolds number Re_1 in Figure 4 is 53,700 and 52,000 for $\Delta T_{fl} = 0$ and $900\ K$, respectively. Re_1 is based on the δ_1 layer thickness, U_o and freestream properties. The difference in Re_1 for these cases reflects the reduced layer width with heat addition.

Thermal expansion and baroclinic torque play an important role in the development of the mixing layer. To show more clearly their effects, Figure 6 presents contour plots of the filtered vorticity, density and temperature for the case of $\phi = 1$ and $\Delta T_{fl} = 900\ K$ but with the effect of baroclinic torque removed as described earlier. Comparing this figure with Figure 4 shows that, without baroclinic torque, the vorticity field is very similar in structure to the case without heat release. The large scale structures are more circular and do not appear to be elongated in the streamwise direction. The regions of high positive vorticity observed in Figure 4b are no longer present when baroclinic torque is removed. However, Figure 6 does show that the vorticity magnitude and rotation rate of the large scale structures are reduced owing to thermal expansion as discussed earlier. The Reynolds number in Figure 6 is $\mathrm{Re}_1 = 60,600$, indicating the layer is thicker in the absence of baroclinic

torque than it is for the case without heat release. This thickening is also a result of thermal expansion.

The trends observed in Figure 6 have also been observed in the pre-transitional DNS simulations of Higuera and Moser (1994). These results suggest that baroclinic torque is the dominant mechanism for mixing layer width reduction with heat release. The results also suggest that thermal expansion in shear layers at high Reynolds number and low Mach number acts to thicken the layer. This statement, however, applies only to naturally or artificially *forced* shear layers. Shear layers developing from laminar inflow conditions may be inhibited by thermal expansion. The initialization described in section 6 for the present simulations attempts to model natural forcing or turbulence shortly downstream of a splitter plate in high Reynolds number experiments.

This conclusion with regard to the role of thermal expansion in shear layers is at variance with the conclusion reached by Soteriou and Ghoniem (1994a). They simulated spatially developing forced mixing layers with heat release using DNS based on a Lagrangian solution scheme for the vorticity transport equation. Soteriou and Ghoniem (1994a) conducted simulations in which they systematically eliminated the effects of thermal expansion and baroclinic torque. They found both these effects to result in shear layer thinning. However, they suggested that thermal expansion plays a more significant role in this growth reduction. Their simulations also showed the vortex structures to be elliptical in shape in the absence of baroclinic torque.

The conclusions reached by Soteriou and Ghoniem (1994a) on the effect of thermal expansion in shear layer development may be resolved with the conclusions reached in this study by recognizing the effect of streamwise pressure gradients. The simulations of Soteriou and Ghoniem (1994a) were conducted in a confined channel. As a consequence, thermal expansion induced streamwise acceleration and in turn a favorable streamwise pressure gradient. Hermanson and Dimotakis (1989) studied the effect of streamwise pressure gradient on shear layer growth by adjusting the test section side wall angle in their experiments. They found that favorable pressure gradients in reacting mixing layers with heat release result in a reduction of layer growth. Therefore, the shear layer thinning and large scale vortex distortion observed in the simulations of Soteriou and Ghoniem (1994a) without baroclinic torque are likely due to the secondary effect of streamwise pressure gradient induced by thermal expansion. In the absence of such a gradient, as in the present simulations, the primary effect of thermal expansion is to thicken the shear layer without greatly distorting the structure of the large scales.

The contour plot of temperature in Figure 5 is equivalent to a plot of the filtered subgrid product. This is a result of the assumptions used in this section with respect to the chemistry. This plot is qualitatively very similar to filtered product plots for the negligible heat release/decoupled simulations described in Calhoon and Menon (1996). Figure 5 shows the peak product to be distributed within the large scale structures. The figure also reveals that product is formed in the braid regions between these structures but at lower levels.

Streamwise averaged temperature, or equivalently product, for the heat release simulations are also similar in form to the results obtained in Calhoon and Menon (1996). Figure 7 presents a plot of the mean normalized streamwise temperature at $\tau = 11$ for $\phi = 1$ and $\Delta T_{fl} = 0$, 300, 600, and 900 K. ΔT in the figure is equal to $T - T_o$. Included in this figure are the experimental results of Hermanson and Dimotakis (1989) (hereafter referred to as H-D) for hydrogen-fluorine mixing layer flames with constant freestream properties and zero streamwise pressure gradient. Also included in Figure 7 are the results for $\phi = 1$ and $\Delta T_{fl} = 900$ K but with the effect of baroclinic torque removed as described earlier.

From 7 it is evident that the mean profiles are approximately symmetric and that the stoichiometric value of temperature/product is not realized in the mean. Figure 7 also shows that 1) the mean temperature profile is not greatly affected by heat release and 2) the peak mean temperature exhibits a slight decreasing trend with increasing heat release. These two qualitative trends have also been observed in the heat release experiments of H-D. Quantitatively, the figure shows the present results to be in excellent agreement with the experimental data. However, the magnitude of the peak mean temperature is slightly underpredicted. The case without baroclinic torque agrees well with the other simulations at the edges of the layer but shows lower peak values at the centerline. This result has implications on the effect of baroclinic torque on product formation as will be discussed shortly.

The results in Figure 7 imply an increasing trend in the mean absolute temperature with increasing heat release. This also implies a decreasing trend in the mean shear layer density. Changes in the mean density may be quantified in terms of the mean normalized density reduction $\Delta\rho/\rho_1$, given in equations (29) and (30). This quantity has been measured by H-D and is plotted in Figure 8. The present results are for $\phi = 1$ and $1/4$, while the experimental results are for $\phi = 1$, $1/2$ and $1/4$. The present data are calculated for each case at a time of $\tau = 11$ as in Figure 7. It is apparent from the figure that the present predictions are is excellent agreement with the experimental data. The simulations have captured the decreasing slope of this curve with increasing flame temperature. H-D speculated that this behavior is a result of alternating hot and cold fluid passing the measuring probe in their experiments. They suggested the hot fluid resulted from product formed in the large scale structures while the cold fluid resulted from the entrainment of pure fluid "tongues" deep into the layer. This picture of shear layer structure is qualitatively supported by the filtered density contours in Figure 5a. In the large

structures, $\rho \rightarrow 0$ as $\Delta T_{fl} \rightarrow \infty$ while the density in cold tongues remain at the freestream value. As a result, the mean density, and thereby $\Delta\rho/\rho_1$, approaches a limiting value with increasing ΔT_{fl}, explaining the trend seen in Figure 8 (Hermanson and Dimotakis, 1989).

H-D also suggested that the mean density reduction is not a function of ϕ, based on their experimental results shown in Figure 8. However, the present results show $\Delta\rho/\rho_1$ to be a weak function of ϕ. As seen in the figure, the predicted variation is within the scatter of the experimental data. It may, therefore, be concluded that the variation of $\Delta\rho/\rho_1$ with ϕ in the experiments of H-D has been obscured by the scatter of their data.

Of great interest in the design community is the effect of various parameters on the total product formation in turbulent shear layers. In Calhoon and Menon (1996) the effects of Reynolds and Damköhler number on product formation have been examined computationally. Also of interest is the effect of heat release on product generation. From Figure 4 it has been observed that heat release modifies the structure of the vorticity field. It is also expected that heat release will impact total product formation. One measure of total product formation in mixing layers is the *product mass thickness* δ_P^* (Hermanson and Dimotakis, 1989) given by,

$$\delta_P^* = \int_{-\infty}^{+\infty} \frac{(\langle T\rangle_{mean} - T_o)}{\Delta T_{fl}} \frac{\langle\rho\rangle_{mean}}{\rho_1} dx_2 \qquad (32)$$

Following H-D this expression may be rearranged to yield,

$$\delta_P^* = \frac{T_o}{\Delta T_{fl}} \int_{-\infty}^{+\infty} \frac{\langle T\rangle_{mean} - T_o}{\langle T\rangle_{mean}} dx_2 \qquad (33)$$

For the infinite rate chemistry considered here, δ_P^* is a measure of the total amount of product mass formed in the layer (Hermanson and Dimotakis, 1989). δ_P^* has been measured by H-D in hydrogen-fluorine mixing layer flames. Figure 9 presents a plot of the product mass thickness normalized by δ_1 as a function of the mean density reduction. The present LES-LEMC simulations consider the cases of $\phi = 1$ and $1/4$, while the experimental results of H-D are for $\phi = 1$, $1/2$ and $1/4$. The figure also includes a data point for the simulation with $\phi = 1$ and $\Delta T_{fl} = 900\ K$ but with the baroclinic torque ω_b set to zero. Simulated results for $\phi = 1$ and $1/4$ using a conventional LES subgrid model are also included in Figure 9 for comparison. The conventional model solves a filtered equation for the mixture fraction $\tilde{\xi}$ using a dynamic gradient diffusion model to close the species transport term. Product formation in the conventional model is calculated neglecting all subgrid fluctuations. All simulated data in Figure 9 have been collected at $\tau = 11$.

From Figure 9, the product mass thickness is seen to decay with increasing heat release. As suggested by H-D, the experimental data decays linearly at a rate independent of ϕ for $\Delta\rho/\rho_1 \geq 0.2$. This figure shows that the present LES-LEMC simulation results have accurately captured this trend. The LES-LEMC model accurately predicts not only the magnitude of the data, but more importantly the slope of the linear decay. This gives support to the notion that the LES-LEMC model has accurately accounted for the basic underlying physics of this shear layer configuration. The conventional subgrid model shows reasonable agreement for the magnitude of the data but underpredicts the decay slope by more than 30%. This is not surprising in view of the failure of conventional LES subgrid modeling to accurately predict the variation of the mean mixed fluid across high Reynolds number mixing layers (Calhoon, 1996).

Figure 9 also reveals that the LES-LEMC case with $\omega_b = 0$ gives a result for δ_P^*/δ_1 which is slightly lower than for the case including baroclinic torque. This result appears to suggest that the effect of baroclinic torque is to enhance mixing by the generation of additional vorticity in the flow. However, this result is misleading because δ_1 changes when the effects of baroclinic torque are removed as mentioned earlier. The dimensional value of δ_P^* for the case with $\omega_b = 0$ is actually 15.2% higher than for the more general case. This difference is offset by a 16.5% increase in δ_1 when $\omega_b = 0$ so that the ratio δ_P^*/δ_1 is slightly smaller for $\omega_b = 0$, as seen in Figure 9. This result indicates that baroclinic torque plays a significant role in reducing product formation. This observation is in agreement with the DNS simulations of McMurtry *et al.* (1989) and Soteriou and Ghoniem (1994a).

From equation (32), the decay of the product mass thickness in Figure 9 is a result of changes in the normalized mean temperature and/or mean density. Changes in these quantities are in turn a result of the effects of thermal expansion and baroclinic torque. From the previous discussion, it appears that thermal expansion is a much more effective mechanism than baroclinic torque in reducing product within the layer. With this in mind, it is of interest to determine whether thermal expansion and baroclinic torque induce greater changes in the normalized temperature or density profiles. The form of the mean temperature and product profiles is a function of the distribution of mixed fluid within the layer. The mixed fluid may be quantified in terms of the mean mixed mixture fraction $\langle\xi_m\rangle_{mean}$ given by,

$$\langle\xi_m\rangle_{mean} = \frac{\int_{\varepsilon}^{1-\varepsilon} \xi \langle \mathbf{p}^{sgs}(\xi)\rangle_{mean}\, d\xi}{\int_{\varepsilon}^{1-\varepsilon} \langle \mathbf{p}^{sgs}(\xi)\rangle_{mean}\, d\xi} \qquad (34)$$

where $\langle \mathbf{p}^{sgs}\rangle_{mean}$ is the mean subgrid mixture fraction probability distribution function calculated from all the subgrid fields at a particular x_2 station. $\langle\xi_m\rangle_{mean}$ is a measure of the mean value of the mixed fluid at transverse location in the layer. Note that the integral in equation (34) excludes the pure unmixed fluid outside the range $\varepsilon \leq \xi \leq 1-\varepsilon$. In this study ε is taken as 0.033.

A plot of the variation of $\langle\xi_m\rangle_{mean}$ across the layer for the different levels of heat release with $\phi = 1$ is given in Figure 10. The transverse coordinate in the

figure has been normalized by the mixed fluid probability thickness δ_{Pm} (Calhoon and Menon, 1996). From the figure, all cases exhibit a large scale transverse gradient in $\langle \xi_m \rangle_{mean}$ as observed computationally in the no heat release/decoupled simulations of Calhoon and Menon (1996) and experimentally by Koochesfahani and Dimotakis (1986) and Konrad (1976). The figure also shows that $\langle \xi_m \rangle_{mean}$ is in general unaffected by variations in heat release. Although, some small differences do exist for the different cases. These differences apparently result in the small differences in the mean normalized temperature profiles in Figure 7.

In contrast to $\langle \xi_m \rangle_{mean}$, the mean density across the layer shows large differences for the various levels of heat release. Figure 11 presents a plot of the mean density normalized by the freestream value. As is intuitively expected, the mean density in the layer decreases significantly with increases in heat release. Figures 10 and 11 reveal that the reduction in product mass thickness observed in Figure 9 is primarily a result of decreased density within the shear layer. The reduction of the mean density and the reduction of the layer width shown in Figure 2 imply that heat release reduces the volumetric entrainment of freestream fluid into the layer. This has been observed experimentally by H-D and they cite this entrainment reduction as the primary mechanism producing the behavior of the product mass thickness in Figure 9.

The final topic addressed in this section concerns the coupling of the subgrid heat release to the resolved scales. As mentioned earlier, the simulations in this section use Coupling Method 1 described in section 4.1. As a result, the LES filtered temperature $\tilde{T}$ is determined from equation (26) given $\tilde{e}$ calculated from the filtered energy equation and $\tilde{Y}_k$ calculated from the subgrid using equation (14). $\tilde{T}$ may also be calculated directly from the subgrid using equation (17). As discussed in section 4.1, these two predictions for $\tilde{T}$ should be compared in order to evaluate the effectiveness of the coupling scheme. Also, since the subgrid pressure has been assumed to be equal to a constant reference value, the resolved pressure $\tilde{p}$ calculated from the state equation (9) must also be compared with the assumed pressure.

Figure 12 presents a plot in time of the maximum percentage difference between the predicted values of $\tilde{T}$ from equation (26) and from equation (17) anywhere in the domain for the case with $\phi = 1$ with $\Delta T_{fl} = 900K$. Also included in this figure is the maximum percentage difference between $\tilde{p}$ and the subgrid assumed pressure. The maximum differences in temperature and pressure are seen to fluctuate around 1.5% and 5.5%, respectively. Figure 13 presents a similar plot but for $\phi = 1/4$ with $\Delta T_{fl} = 900K$. The differences for this case fluctuate around 1.5% and 5.% for temperature and pressure, respectively. Figures 14 and 15 present plots of the mean value of these differences calculated in the mixing region for $\phi = 1$ and $1/4$, respectively. The mixing region is taken here as the area in which the filtered subgrid mixture fraction within each cell is $\varphi \leq \tilde{\xi} \leq 1 - \varphi$ where $\varphi = 1\,x\,10^{-6}$. The mean differences in pressure and temperature are seen to be below 1.2% for both cases indicating that the larger fluctuations evident in Figures 12 and 13 are localized. Based on the relatively small magnitudes of the differences seen in Figures 12–15, the subgrid heat release has been properly coupled to the resolved scales using Coupling Method 1. The small temperature differences also indicate that solution of the LES filtered energy equation is redundant and may be eliminated. Consequently, Coupling Method 2 described in section 4.1 is also appropriate for these problems.

The differences in the predictions for pressure and temperature from the subgrid and resolved scales are also an indirect measure of the truncation errors realized in the volume expansion scheme described in section 5. Errors introduced from the truncation will also appear in the temperature and pressure differences in Figures 12–15. In view of the relatively small differences seen in these figures and the good agreement of the present results with experiment data in other figures, the truncation errors in these simulations are believed to be small. This is a result of the moderate heat release levels considered in this section. For higher heat release, however, the truncation error may become large. This situation may be remedied by generalizing the LES-LEMC algorithm to includes a variable number of subgrid elements within each LES cell (Calhoon, 1996). In this case no truncation is necessary and the associated errors are eliminated.

7.2 Heat Release with Variable Freestream Properties

In the previous section the freestream mean molecular weights and mixture specific heats at constant pressure were assumed to be the same on both sides of the mixing layer. With these assumptions, the contributions from the temperature-species correlations T_k^{sgs} in the state equations are negligible, as previously mentioned. Relaxing these assumptions, T_k^{sgs} may play a significant role in the calculation of the pressure and temperature. However, these correlations are generally neglected in LES simulations of reacting flows without justification. Brizuela (1995) found temperature-species correlations to be significant using an assumed pdf model in the context of Reynolds averaged simulation. Neglecting contributions from T_k^{sgs} in the context of LES may also result in substantial errors. In this section, contributions from these terms are evaluated using the LES-LEMC model.

The simulations presented in this section relax the assumption of equal properties in the fuel and oxidizer freestreams in order to assess the effect of temperature-species correlations in mixing layers. In these simulations, species F and O are not diluted. The molecular weights of F and O are again taken to be equal to those of hydrogen and fluorine, respectively. The reaction chem-

istry, freestream temperature and pressure, flow field and subgrid initialization, etc. are the same in these simulations as in the previous section, accounting, of course, for the differences in the freestream properties. The viscosity is also approximated using equation (21) with the same values of $C_{\mu,1}$ and $C_{\mu,2}$ used in the previous section. With the change in freestream properties, the Reynolds number $\mathrm{Re}_{\omega,o}$ based on the fuel stream density decreases to 980. Basing $\mathrm{Re}_{\omega,o}$ on the oxidizer stream density gives a value of 18,500. The density ratio ρ_2/ρ_1 for this case is 18.8, which is quite large. With $U_o = 71\ m/\mathrm{sec}$, the convective Mach number M_c is 0.044.

Heat release levels for the simulations are $\Delta T_{fl} = 450$ and 900 K. Subgrid heat release is coupled to the resolved scales using Coupling Method 2, described in section 4.1. As a result, the filtered energy equation for $\bar{\rho}\tilde{E}$ is eliminated and $\tilde{T}$ is calculated from the subgrid using equation (17). The reason behind the choice of this coupling scheme will be discussed later in this section.

Figure 16 and 17 present contour plots of the filtered vorticity and temperature fields for both $\Delta T_{fl} = 450$ and 900 K at $\tau = 11$. The qualitative structure of the vorticity field shown in Figure 16 is similar to the structure seen in Figure 4. The large scale structures are somewhat elliptical in shape and positive vorticity generated by baroclinic torque is evident. However, higher levels of positive vorticity occur on the lower side of the layer where the flame resides, as shown in Figure 17.

The shift of the flame to the lower side of the layer seen in Figure 17 results from a low value of stoichiometric mixture fraction ξ_{st}. For the conditions of these simulations, $\xi_{st} = 0.0504$ due to the low molecular weight of species F. Figure 17 also shows the flame to shift toward the left-hand side of the large scale structures. This streamwise shift of the flame is similar to what was observed by Calhoon and Menon (1996) for the zero heat release/decoupled simulations. The streamwise flame shift results from a streamwise gradient in the mean mixed mixture fraction within the large scale structures (Calhoon and Menon, 1996).

A previously mentioned, subgrid temperature-species correlations appear in the state equations (9) and (26). These equations may be rewritten as,

$$\bar{p} = \bar{\rho} R^{\circ} \left(\Lambda_o^* + \Lambda^* \right) \tag{35}$$

$$\tilde{e} = \sum_{k=1}^{K} \tilde{Y}_k \left(\Delta h_k^{\circ} - c_{p,k} T^{\circ} \right) + \Gamma_o^* + \Gamma^* \tag{36}$$

where,

$$\Lambda_o^* = \sum_{k=1}^{K} \frac{\tilde{T}\tilde{Y}_k}{W_k} \tag{37}$$

$$\Lambda^* = \sum_{k=1}^{K} \frac{T_k^{sgs}}{W_k} \tag{38}$$

$$\Gamma_o^* = \sum_{k=1}^{K} \left(c_{p,k} + \frac{R^{\circ}}{W_k} \right) \tilde{T}\tilde{Y}_k \tag{39}$$

$$\Gamma^* = \sum_{k=1}^{K} \left(c_{p,k} + \frac{R^{\circ}}{W_k} \right) T_k^{sgs} \tag{40}$$

The ratios Λ^*/Λ_o^* and Γ^*/Γ_o^* indicate the relative importance of the contributions of the subgrid to the filtered pressure and internal energy.

Figure 18 presents a contour plot of the ratio Λ^*/Λ_o^* for both mixing layer flames. Values of $\tilde{Y}_k$, T_k^{sgs} and $\tilde{T}$ in equations (37) and (38) are calculated from the subgrid fields using equations (14), (15) and (17), respectively. The ratio Λ^*/Λ_o^* represents an error in the calculation of $\bar{p}$ when T_k^{sgs} is neglected. From the figure it is apparent that the subgrid fluctuations make a significant contribution to $\bar{p}$. Large negative values as low as -20% occur in the vicinity of the flame for $\Delta T_{fl} = 900\ K$. For $\Delta T_{fl} = 450\ K$, values as low as -13% are realized. Contours plots of the ratio Γ^*/Γ_o^* appear almost identical to Figure 18 and show similar magnitudes. Neglecting the temperature-species correlations, as is common practice in LES, is, therefore, unjustifiable for cases in which the mean molecular weight is not constant. Discarding these correlations in conventional LES modeling can result in large errors in the calculation of the filtered pressure and temperature. This is true even for low heat release flames such as the $\Delta T_{fl} = 450\ K$ case considered here. In this simulation, the normalized adiabatic flame temperature rise $\Delta T_{fl}/T_o$ is only 1.5. However, errors of 13% may still be realized in the filtered pressure for this case.

From Figure 18, large magnitudes in Λ^*/Λ_o^* are seen to be distributed around the large scale structures and in the braid regions between structures. In these regions, the subgrid mixture fraction variance is large. Within the large structure cores, Λ^*/Λ_o^* is more uniformly distributed with lower values because small scale mixing has more time to eliminate scalar gradients. Λ^*/Λ_o^* is negative over most of the layer but Figure 18 also reveals positive correlations in the immediate vicinity of the flame. These positive correlations also appear in the mean profile of Λ^* presented in Figure 19. On the lower side of the layer, a relatively small positive peak in $\langle \Lambda^* \rangle_{mean}$ is present. Over the rest of the layer, $\langle \Lambda^* \rangle_{mean}$ is negative with large magnitude. The double minimum structure of the $\langle \Lambda^* \rangle_{mean}$ profiles is a result of the distribution of Λ^* around the large scale vortices seen in Figure 18. This structure is in qualitative agreement with the mixing layer passive scalar statistics of Fiedler (1974).

The large negative values of Λ^* seen in Figures 18 and 19 result from negative correlations for the fuel species. This is evident from Figure 20 which is a plot of the contributions to $\langle \Lambda^* \rangle_{mean}$ from each species. The large negative correlations for F dominate $\langle \Lambda^* \rangle_{mean}$ over most of the layer. The relatively large magnitude results from this species' low molecular weight. The oxidizer correlation is also negative but has a much lower magnitude

due to the high molecular weight of this species. Negative correlations for the reactant species are expected since positive temperature fluctuations will be accompanied by consumption of the reactants. The product species correlation, on the other hand, is always positive as seen in Figure 20. The positive correlation for P at the edge of the layer on the lower side results in the positive peak in $\langle\Lambda^*\rangle_{mean}$ seen in Figure 19. The remainder of the layer is dominated by the negative correlations for F.

The subgrid heat release in these simulations is coupled to the resolved scales using Coupling Method 2 of section 4.1. Since the resolved scale temperature is calculated directly from the subgrid, this approach only requires that the predicted filtered pressure, calculated from equation (9), be compared to the assumed subgrid pressure to verify the coupling. Figure 21 presents a plot in time of the maximum percent difference between these two values of pressure anywhere in the domain. The pressure difference is found to fluctuate around $\approx 3.5\%$ near the end of the simulation. Also, the mean value of the pressure difference in the mixing region is below 0.7% for both simulations. With these small differences, the subgrid heat release is, therefore, properly coupled to the resolved scales.

Simulations for these two cases have also been carried out using Coupling Method 1 to couple subgrid heat release to the resolved scales. In these simulations, however, this coupling approach failed. This was apparent from large differences in the subgrid and resolved scale predictions for the filtered temperature. Errors of $\approx 25\%$ for the maximum temperature difference were realized. These large differences appeared in regions where the cumulative temperature-species correlation Λ^* was significant. The failure of the coupling could be a result of a breakdown of the assumptions of LEMC subgrid model and/or truncations errors of the subgrid volume expansion algorithm. However, this is not likely the case because large coupling errors were not realized in the simulations of the previous section for the same flow configuration. The only difference between the simulation of this section and the previous one is the difference in specification of the freestream properties. If the LEMC assumptions and truncation errors were the source of the problem, large temperature differences would be expected along the entire length of the flame. However, the large temperature differences in these simulations were primarily realized only in regions of the flame where Λ^* was significant.

A plausible explanation for the failure of Coupling Method 1 is the breakdown of the subgrid model for the total enthalpy flux term H_j^{sgs} in the filtered energy equation. Poor estimation of H_j^{sgs} using the gradient diffusion assumption/eddy viscosity model in equation (18) will degrade the prediction of $\tilde{e}$ from the filtered energy equation, resulting in errors in the calculation of $\tilde{T}$ from equation (36). Expanding the exact form of H_j^{sgs} in equation (4) reveals that this term contains velocity-temperature-species correlations. The influence of these correlations may not be well represented by the model given in equation (18). These velocity-temperature-species correlations are expected to be large in these flames due to the large difference in the mean molecular weight of the freestreams. Improperly accounting for these correlations in the filtered energy equation will result in errors in the prediction $\tilde{T}$ and, in turn, failure of the coupling. This explanation is consistent with the fact that the large temperature differences primarily occur in regions where Λ^* is significant.

The failure of Coupling Method 1 in this section illustrates the principle advantage of Coupling Method 2. Coupling Method 2 obviates the need to solve the filtered energy equation for $\bar{\rho}\tilde{E}$. As a consequence, this method eliminates the need to model H_j^{sgs}, avoiding the uncertainties associated with the eddy viscosity model given by equation (18).

8 Conclusions

The LES-LEMC method has been applied to describe diffusion flame structure in turbulent reacting mixing layers. This approach includes a more fundamental treatment of the effects of molecular diffusion, chemical reactions and small scale turbulent stirring than other LES closure techniques. This has been accomplished by way of the linear eddy mixing model. The LES-LEMC methodology has been applied to mixing and reaction in turbulent mixing layers with chemical heat release. The analysis of the simulation results leads to the following conclusions:

1. The present LES-LEMC modeling approach has captured many of the qualitative trends observed in high Reynolds number turbulent reacting mixing layers. This approach has also yielded good quantitative agreement for several important quantities that have been measured experimentally for both infinite and finite rate chemistry and for cases with and without heat release. Specifically, in a previous study (Calhoon and Menon, 1996), the LES-LEMC method has quantitatively captured the variation of product thickness with respect to Reynolds number and Damköhler number. In this study, the method has quantitatively captured the variation of product thickness with respect heat release parameter. In addition, these results have been produced using a single value of the model calibration coefficient. To the author's knowledge, no other combustion model has demonstrated the present level of quantitative accuracy in predicting the variation of product thickness with these parameter.

2. Baroclinic torque is found to be the primary mechanism for the thinning of low Mach number, high Reynolds number reacting mixing layers with heat

release. However, baroclinic torque plays only a small role in the reduction of product mass generation in these layers.

3. Volumetric expansion due to heat release does not play a role in the thinning of forced (either naturally or artificially) high Reynolds number mixing layers in a zero streamwise pressure gradient environment. Volumetric expansion is found to actually cause layer thickening in the absence of baroclinic torque. This conclusion is in contrast to the conclusion of other researchers who found the opposite trend. A thinning trend attributed to volumetric expansion by other researchers is found to actually be a result of an induced streamwise pressure gradient in their simulations.

4. The large scale distribution of mixed fluid within high Reynolds number reacting mixing layers is found to be approximately invariant with changes in the level of heat release. The reduction of product mass with increasing heat release is found to be primarily a result of density reduction in the layer resulting from heat release and volume expansion.

5. The assumption generally employed in LES subgrid modeling that temperature-species correlations are negligible is not justified for diffusion flame simulations in which significant differences exist between the freestream mean molecular weights. These correlations may be large even for low heat release simulations. Neglecting these correlations may result in large errors in the calculation of the resolved scale pressure and temperature.

ACKNOWLEDGMENT

This work was supported in part by the Air Force Office of Scientific Research under the Focussed Research Initiative Contract No. 200-1Q-14N44085. Support for some of the computations was provided by the DOD High Performance Computing Centers at Wright Patterson AFB (Paragon) and the Army Research Laboratory (SGI Power Challenge) and is gratefully acknowledged.

REFERENCES

Baum, M., Poinsot, M.B. and Thevenin, D. (1994), Accurate Boundary Conditions for Multicomponent Reactive Flows, *J. Comp. Phys.*, **116**, pp. 247-261.

Bayliss, A., Parikh, P., Maestrllo, L., and Turkel, E. (1985), A Fourth-Order Scheme for the Unsteady Compressible Navier-Stokes Equations, ICASE Report No. 85-44.

Breidenthal, R. (1981), Structure in Turbulent Mixing Layers and Wakes Using a Chemical Reaction, *J. Fluid Mech.*, **109**, pp. 1–24.

Brizuela, E. A. (1995), Errors Due to Correlations in Evaluating Mean Density for Favre-Averaged Enthalpy and Composition in Turbulent Reactive Flow, *Comb. and Flame*, **103**, 4, pp. 343–347.

Calhoon, W.H. Jr., Menon, S., and Goldin, G.M. (1995), Comparison of Reduced and Full Chemical Mechanisms for NO_x Prediction in Nonpremixed Turbulent H_2-Air Jet Flames, *Comb. Sci. Tech.*, **104**, pp. 115–141.

Calhoon, W.H. Jr. (1996), On Subgrid Combustion Modeling for Large-Eddy Simulations, Ph.D. Thesis, Georgia Institute of Technology, Atlanta, Ga.

Calhoon, W.H. Jr. and Menon, S. (1996), Subgrid Modeling for Reacting Large Eddy Simulations, presented at the 34th Aerospace Sciences Meeting, Reno, Nevada, AIAA paper 96-0516.

Dimotakis, P.E. (1989), Turbulent Free Shear Layer Mixing, presented at the 27th Aerospace Sciences Meeting, Reno, Nevada, AIAA paper 89-0262.

Erlebacher, G., Hussaini, M.Y., Speziale, C.G., and Zang, T.A. (1990), Toward the Large-Eddy Simulation of Compressible Turbulent Flows, *ICSE Report*, No. 87–20.

Frankel, S.H., Adumitroaie, V., Madnia, C.K. and Givi, P. (1993), Large Eddy Simulation of Turbulent Reacting Flows by Assumed pdf Methods. In Ragab, S.A. and Piomelli, U., editors, *Engineering Application of Large Eddy Simulations*, pp. 81-101, New York: ASME, FED-Vol. 162.

Fiedler, H. E. (1974), Transport of Heat Across a Plane Turbulent Mixing Layer, *Advances in Geophysics*, **18A**, pp. 93–109.

Fureby, C. (1995), On Reaction Rate Modeling in Large Eddy Simulation of Chemically Reactive Flow, submitted to *Phys. Fluids.*

Fureby, C. and Möller, S.-I. (1995), Large Eddy Simulation of Reacting Flows Applied to Bluff Body Stabilized Flames, *AIAA J.*, **33**, 12, pp. 2339–2347.

Ganji, A. R., and Sawyer, R. F. (1980), Experimental Study of the Flowfield of a Two-Dimensional Premixed Turbulent Flame, *AIAA J.*, **18**, 7, pp. 817–824.

Gao, F., and O'Brien, E.E. (1993), A Large-Eddy Simulation Scheme for Turbulent Reacting Flows, *Phys. Fluids A*, **5**, pp. 1282–1284.

Goldin, G.M. and Menon, S. (1996), A Linear Eddy Model for Steady-State Turbulent Combustion, presented at the AIAA 34th Aerospace Sciences Meeting, Reno, Nevada, AIAA paper 96-0519.

Hariharan, N. and Sankar, L.N. (1994), Higher Order Numerical Simulation of Rotor Flow Field, AHS Forum and Technology Display, Washington, DC., May.

Hariharan, N. (1995), High Order Simulation of Unsteady Compressible Flows Over Interacting Bodies with Overset Grids, Ph.D. thesis, Georgia Institute of Technology.

Hermanson, J. C., Mungal, M. G., and Dimotakis, P. E. (1987), Heat Release Effects on Shear-Layer Growth and Entrainment, *AIAA J.*, **25**. 4, pp. 578–583.

Hermanson, J.C. and Dimotakis, P.E. (1989), Effects of Heat Release in a Turbulent, Reacting Shear Layer, *J. Fluid Mech.*, **199**, pp. 333–375.

Higuera, F.J. and Moser, R.D. (1994). Effect of Chemical Heat Release in a Temporally Evolving Mixing Layer, *Proc. CTR 1994*, pp. 19–40.

Kee, R.J., Rupley, F.M. and Miller, J.A. (1989), Chemkin-II: A Fortran Chemical Kinetics Package for the Analysis of Gas Phase Chemical Kinetics, Sandia National Laboratories Report, SAND89-8009B.

Keller, J. O., and Daily, J. W. (1983), The Effect of Large Heat Release on a Two-Dimensional Mixing Layer, presented at the AIAA 21st Aerospace Sciences Meeting, Reno, Nevada, AIAA Paper 83-0487.

Kerstein, A.R. (1988), Linear-Eddy Model of Turbulent Scalar Transport and Mixing, *Comb. Sci Tech.*, **60**, pp. 391-421.

Kerstein, A.R. (1989), Linear-Eddy Model of Turbulent Transport II. Application to Shear Layer Mixing, *Comb. Flame*, **75**, pp. 397-413.

Kerstein, A.R. (1990), Linear-Eddy Model of Turbulent Transport III. Mixing and Differential Molecular Diffusion in Round Jets, *J. Fluid Mech.*, **216**, pp. 411–435.

Kerstein, A.R. (1991), Linear-Eddy Model of Turbulent Transport. Part 6: Microstructure of Diffusive Scalar Fields. J. Fluid Mech., **231**, pp. 361—394.

Kerstein, A.R. (1992), Linear-Eddy Model of Turbulent Transport 4. Structure of Diffusion-Flames, *Comb. Sci Tech.*, **81**, pp.75–96.

Kim, W.-W. and Menon, S. (1995), On the Properties of a Localized Dynamic Subgrid-Scale Model for Large-Eddy Simulations, submitted to *J. Fluid Mech.*

Konrad, J. H. (1976), An Experimental Investigation of Mixing in Two-Dimensional Turbulent Shear Flows with Application to Diffusion-Limited Chemical Reactions, Ph.D. thesis, California Institute of Technology.

Koochesfahani, M. M., and Dimotakis, P. E. (1986), Mixing and Chemical Reactions in a Turbulent Liquid Mixing Layer, *J. Fluid Mech.*, **170**, pp. 83-112.

Koutmos, P., Mavridis C. and Papailiou, D. (1996), A Study of Turbulent Diffusion Flames Formed by Planar Fuel Injection into the Wake Formation Region of a Slender Square Cylinder, submitted to *Twenty-sixth Symposium (Int.) on Combustion,* Naples, Italy.

Liou, M.-S., and Steffen, C.J. (1993), A New Flux Splitting Scheme, *J. Comp. Phys.*, **107**, pp. 23–39.

Mathey, T. and Chollet, J.P. (1996), Large Eddy Simulation of Turbulent Mixing. In Gavrilakis *et al.*, editors, *Advances in Turbulence,* **6**, pp. 39-42, Kluwer Academic Publishers, The Netherlands.

McMurthy, P.A., Riley, J.J., and Metcalfe, R.W. (1989), Effects of Heat Release on the Large-scale Structure in Turbulent Mixing Layers, *J. Fluid Mech.*, **199**, pp. 297-332.

McMurtry, P.A., Menon, S., and Kerstein, A.R. (1992), A Subgrid Mixing Model for Nonpremixed Turbulent Combustion, presented at the AIAA 30th Aerospace Sciences Meeting, Reno, Nevada, AIAA paper 92-0234.

McMurtry, P.A., Gansauge, T.C., Kerstein, A.R. and Krueger, S.K. (1993), Linear Eddy Simulations of Mixing in a Homogeneous Turbulent Flow, *Phys. Fluids A*, **5**, 4, pp. 1023–1034.

Menon, S. (1991), Active Control of Combustion Instability in a Ramjet Using Large-Eddy Simulations, presented at the AIAA 29th Aerospace Sciences Meeting, Reno, Nevada, AIAA paper 91-0411.

Menon, S., and Jou, W.H. (1991), Large-Eddy Simulations of Combustion Instability in an Axisymmetric Ramjet Combustor, *Comb. Sci. Tech.*, **75**, pp. 53-72.

Menon, S., McMurtry, P.A., and Kerstein, A.R. (1993a), A Linear Eddy Subgrid Model for Turbulent Combustion: Application to Premixed Combustion, presented at the AIAA 31st Aerospace Sciences Meeting, Reno, Nevada, AIAA paper 93-0107.

Menon, S., McMurtry, P.A., and Kerstein, A.R. (1993b), A Linear Eddy Subgrid Model for Turbulent Combustion: Application to Premixed Combustion. In Galperin, B. and Orszag, S.A., editors, *Large Eddy Simulation of Complex Engineering and Geophysical Flows*, pp. 287–314, Cambridge University Press, Cambridge.

Menon, S. and Calhoon, W.H. Jr. (1996), Subgrid Mixing and Molecular Transport Modeling in a Reacting Shear Layer, *Twenty-sixth Symposium (Int.) on Combustion,* The Combustion Institute, in press.

Michalke, A. (1964), On the Inviscid Instability of the Hyperbolic-Tangent Velocity Profile, *J. Fluid Mech.*, **19**, 4, pp. 543–556.

Moin, K, Squires, W., Cabot, W. and Lee, S. (1991), A Dynamic Subgrid-Scale Model for Compressible Turbulence and Scalar Transport, *Phys. Fluids A*, **3**, 11, pp.2746–2757.

Mungal, M.G., and Dimotakis, P.E. (1984), Mixing and Combustion with Low Heat Release in a Turbulent Shear Layer, *J. Fluid Mech.*, **148**, pp. 349–382.

Nelson, C.C. (1995), Private communication.

Park, K.-H., Metcalfe, R. W., and Hussain, F. (1994), Role of Coherent Structures in an Isothermally Reacting Mixing Layer, *Phys. Fluids*, **6**, 2, pp. 885–902.

Pitz, R. W., and Daily, J. W. (1983), Combustion in a Turbulent Mixing Layer Formed at a Rearward-Facing Step, *AIAA J.* , **21**, 11, pp. 1565–1570.

Pope, S.B. (1979), The Statistical Theory of Turbulent Flames, *Phil. Trans. Royal Soc. London*, **291**, pp. 529–568.

Pope, S. B. (1985), PDF Methods for Turbulent Reacting Flows, *Progress in Energy and Combustion Science*, Vol. 11, pp. 119–192.

Pope, S. B. (1990), PDF Methods for Turbulent Combustion: Progress and Challenges, *Twenty-Third Symposium (Int.) on Combustion*, The Combustion Institute, pp. 591–612.

Riley, J.J., and Metcalfe, R.W. (1980), Direct Numerical Simulations of a Perturbed, Turbulent Mixing Layers, presented at the AIAA 18th Aerospace Sciences Meeting, Pasadena, California, AIAA paper 80-0274.

Roshko, A. (1976), Structure of Turbulent Shear Flows: A New Look, *AIAA J.*, **14**, 10, pp. 1349–1357.

Schumann, U. (1989), Large-Eddy Simulation of Turbulent Diffusion with Chemical Reactions in the Convective Boundary Layer, *Atmos. Env.*, **23**, 8, pp. 1713–1727.

Soteriou, M. C., and Ghoniem, A. F. (1994a), The Vorticity Dynamics of an Exothermic, Spatially Developing, Forced, Reacting Shear Layer, *Twenty-Fifth Symposium (Int.) on Combustion*, The Combustion Institute, pp. 1265–1272.

Soteriou, M. C., and Ghoniem, A. F. (1994b), Dynamics of Reacting Shear Flows; Effects of Exothermicity and Forcing, presented at the AIAA 32nd Aerospace Sciences Meeting, Reno, Nevada, AIAA Paper 94-0777.

Sykes, R.I., Henn, D.S., and Parker, S.F. (1992), Large-Eddy Simulation of a Turbulent Reacting Plume, *Atmos. Env.*, **26A**, 14, pp. 2565–2574.

Smith, T.M., Menon, S., and McMurtry, P.A. (1994), The Structure of Premixed Flames in Isotropic and Shear Driven Turbulent Flows, presented at the 32nd Aerospace Sciences Meeting, Reno, Nevada, AIAA paper 94-0677.

Tennekes, H. and Lumley, J.L. (1972), A First Course in Turbulence, MIT Press, Cambridge, MA.

Williams, F.A. (1985), Combustion Theory, 2nd ed., The Benjamin/Cummings Publishing Company, Menlo Park, CA.

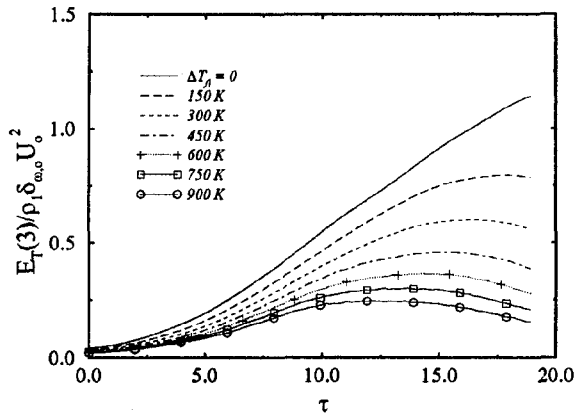

Figure 1. Temporal evolution of the layer energy in the third spatial mode for $\phi = 1$ and different levels of heat release.

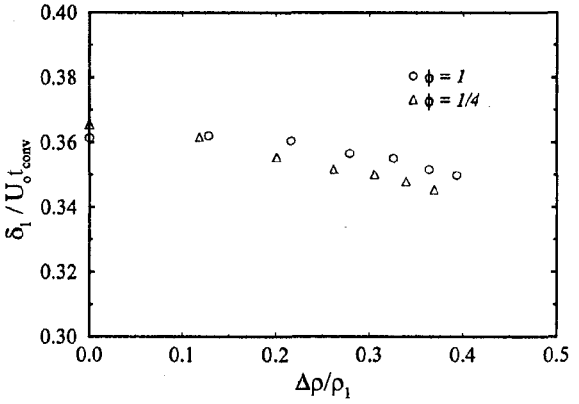

Figure 2. Variation of the mixing layer thickness δ_1 (based on the mean temperature profile) with heat release at $\tau = 11$.

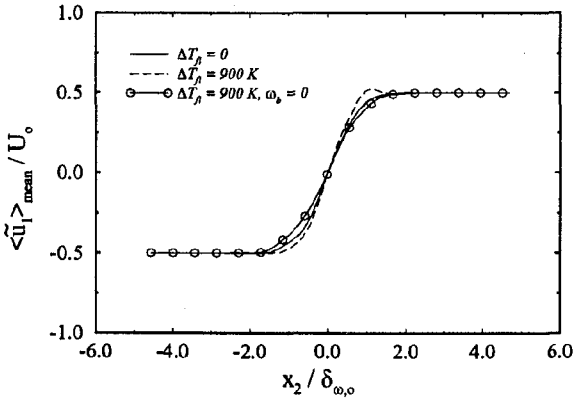

Figure 3. Mean streamwise velocity profiles at $\tau = 11$ for heat release levels of $\Delta T_{fl} = 0$ and 900 K with $\phi = 1$. Baroclinic torque effects removed for the case with $\omega_b = 0$.

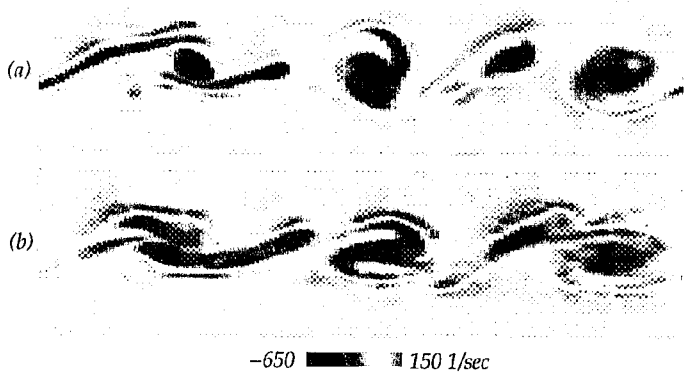

Figure 4. Filtered vorticity contours at $\tau = 11$ for $\phi = 1$. (a) $\Delta T_{fl} = 0$; (b) $\Delta T_{fl} = 900\ K$.

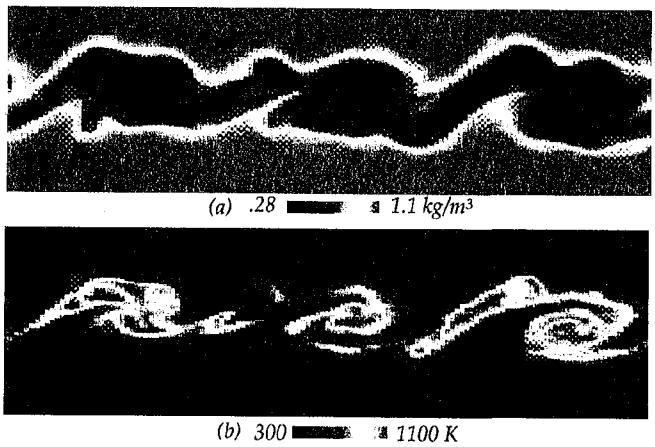

Figure 5. Contours of filtered subgrid (a) density and (b) temperature at $\tau = 11$ for $\phi = 1$ and $\Delta T_{fl} = 900\ K$.

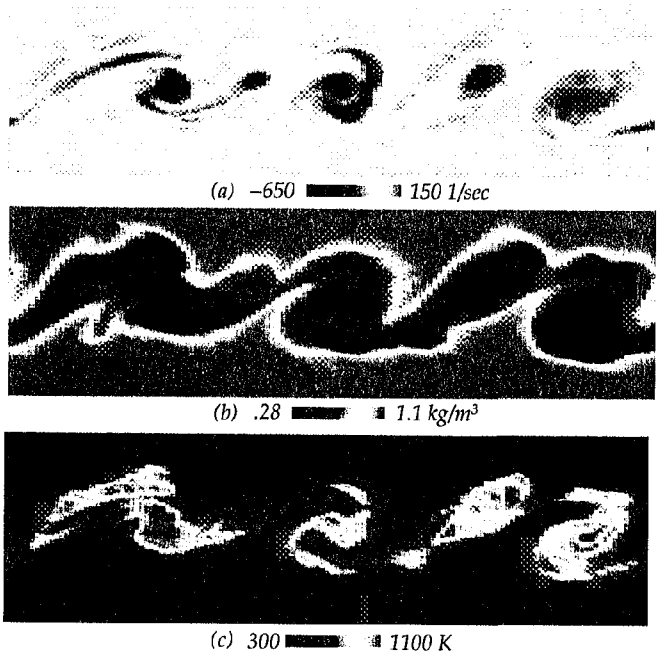

Figure 6. Contours of filtered (a) vorticity, (b) subgrid density and (c) subgrid temperature at $\tau = 11$ for $\phi = 1$, $\Delta T_{fl} = 900\ K$ and no baroclinic torque effects.

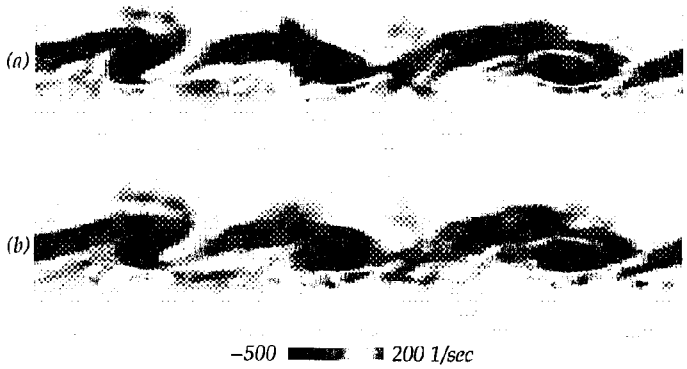

Figure 16. Filtered vorticity contours at $\tau = 11$ for pure fuel and oxidizer freestreams. (a) $\Delta T_{fl} = 450\ K$; (b) $\Delta T_{fl} = 900\ K$.

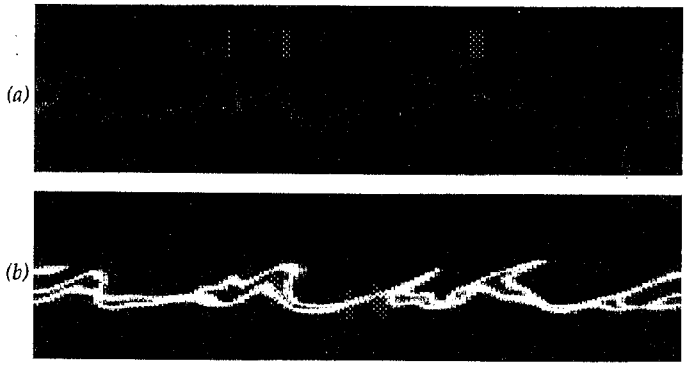

Figure 17. Filtered subgrid temperature contours at $\tau = 11$ for pure fuel and oxidizer freestreams. (a) $\Delta T_{fl} = 450\ K$; (b) $\Delta T_{fl} = 900\ K$.

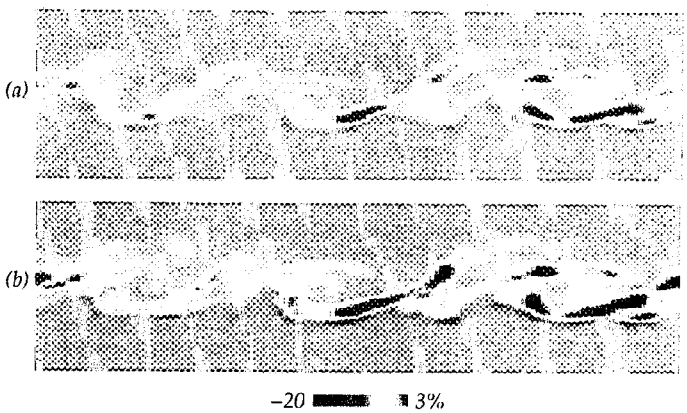

Figure 18. Contours of normalized cumulative subgrid temperature–species correlations, Λ^*/Λ^*_O, at $\tau = 11$ for pure fuel and oxidizer freestreams. (a) $\Delta T_{fl} = 450\ K$; (b) $\Delta T_{fl} = 900\ K$.

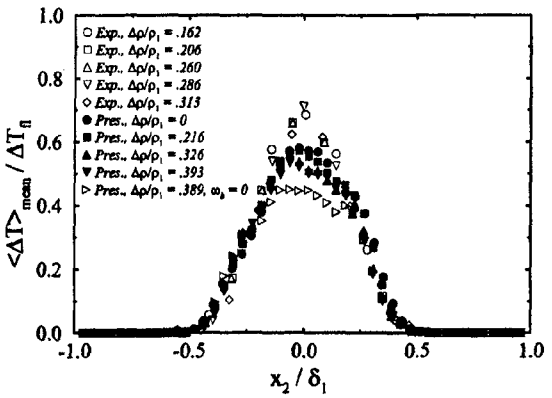

Figure 7. Mean normalized temperature rise across the mixing layer for $\phi = 1$. Experimental results are from Hermanson and Dimotakis (1989). Present results are for cases with $\Delta T_{fl} = 0$, *300*, *600* and *900 K* which have mean density reduction values of *0*, *.216*, *.326* and *.393*, respectively. For the case with no baroclinic torque ($\omega_b = 0$), $\Delta T_{fl} = 900$ *K* and $\Delta\rho/\rho_1 = .389$. All simulated results at $\tau = 11$.

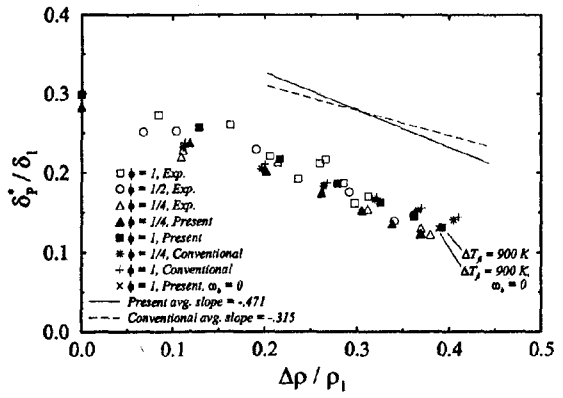

Figure 9. Variation of the normalized product mass thickness with heat release. Experimental results are from Hermanson and Dimotakis (1989). Simulated results for both the present LES–LEMC subgrid model and conventional LES subgrid closure are included. The conventional model uses a gradient diffusion/eddy viscosity transport model of ξ and assumes perfect subgrid mixing. Also included are LES–LEMC results for $\Delta T_{fl} = 900$ *K*, $\phi = 1$ and no baroclinic torque. All simulated results at $\tau = 11$. Average slopes for the present and conventional simulations calculated from data in the range $.1 \le \Delta\rho/\rho_1 \le .45$ and for both values of ϕ.

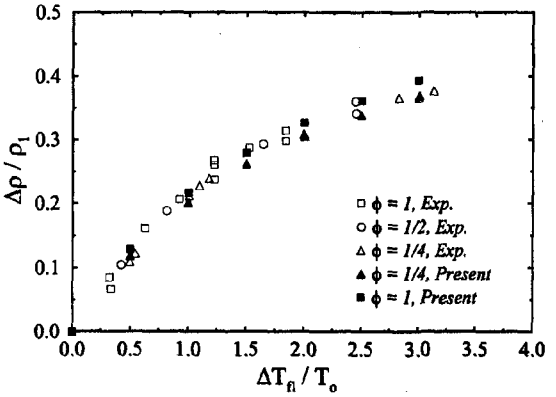

Figure 8. Variation of the mean density reduction with the adiabatic flame temperature rise. Experimental results are from Hermanson and Dimotakis (1989). Present results at $\tau = 11$.

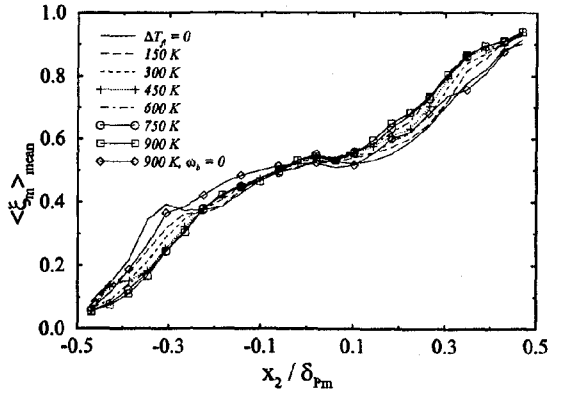

Figure 10. Averaged mean mixed mixture fraction across the layer for various levels of the heat release; $\phi = 1$ and $\tau = 11$.

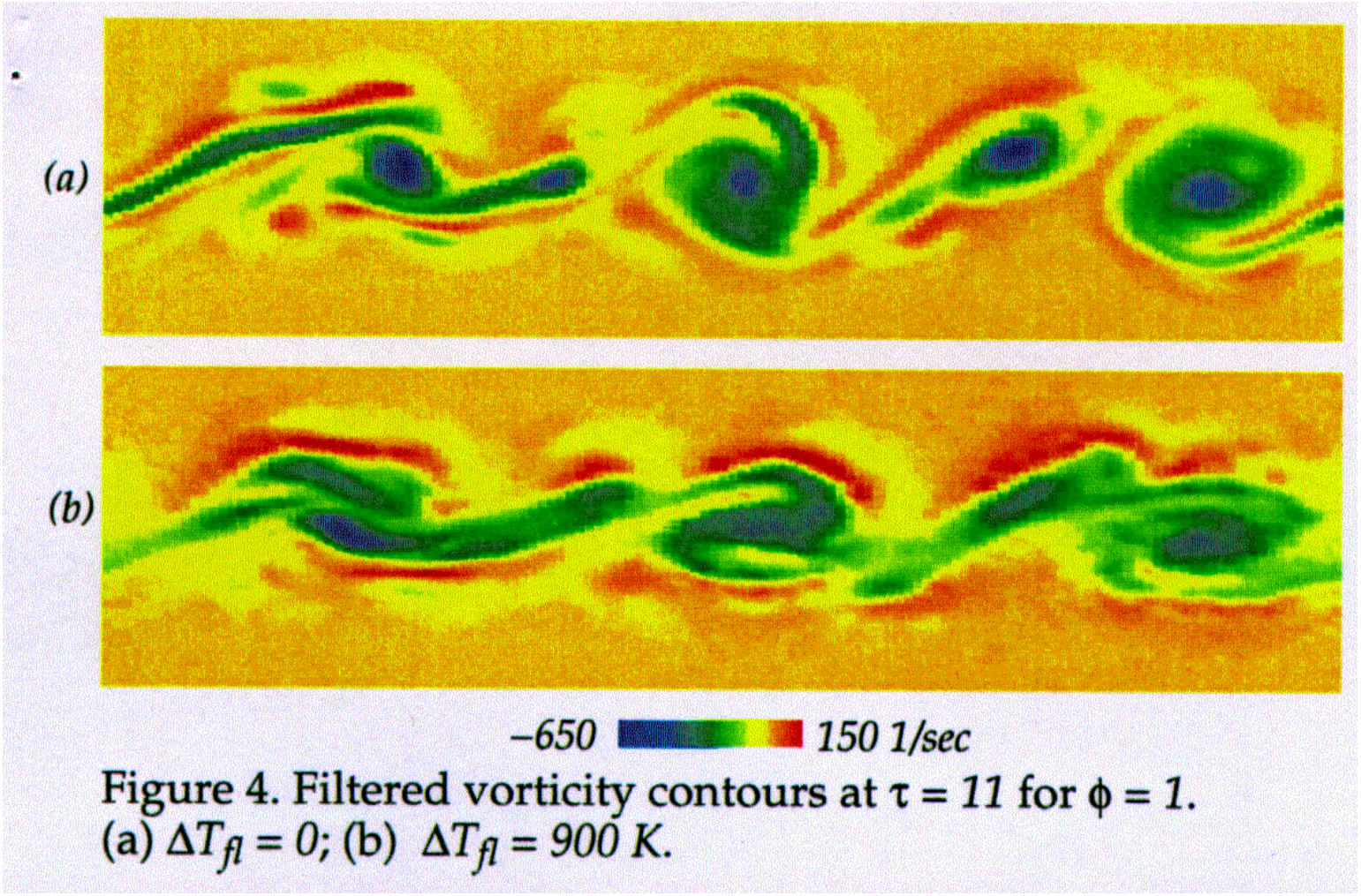

Figure 4. Filtered vorticity contours at $\tau = 11$ for $\phi = 1$.
(a) $\Delta T_{fl} = 0$; (b) $\Delta T_{fl} = 900$ K.

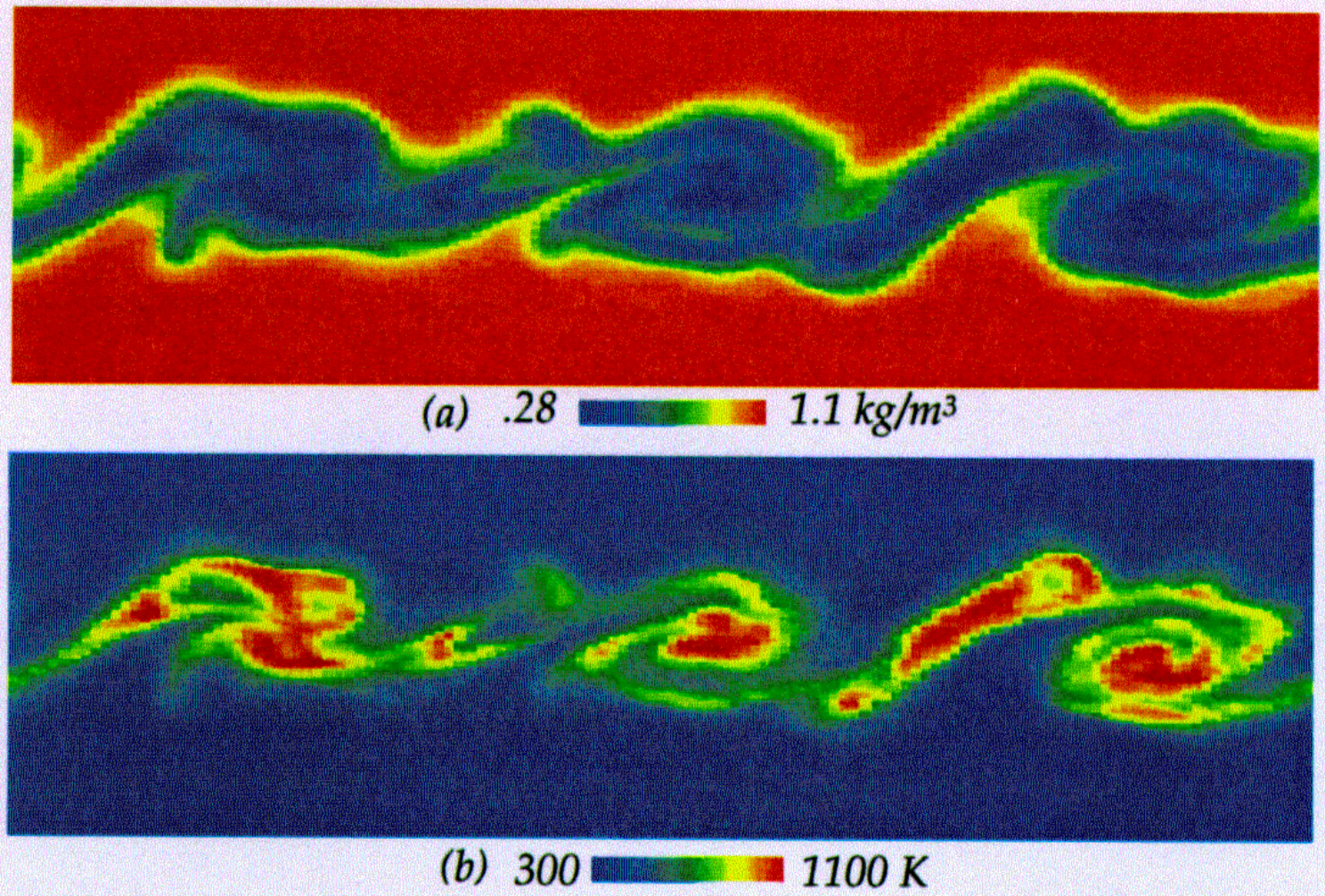

Figure 5. Contours of filtered subgrid (a) density and (b) temperature at $\tau = 11$ for $\phi = 1$ and $\Delta T_{fl} = 900$ K.

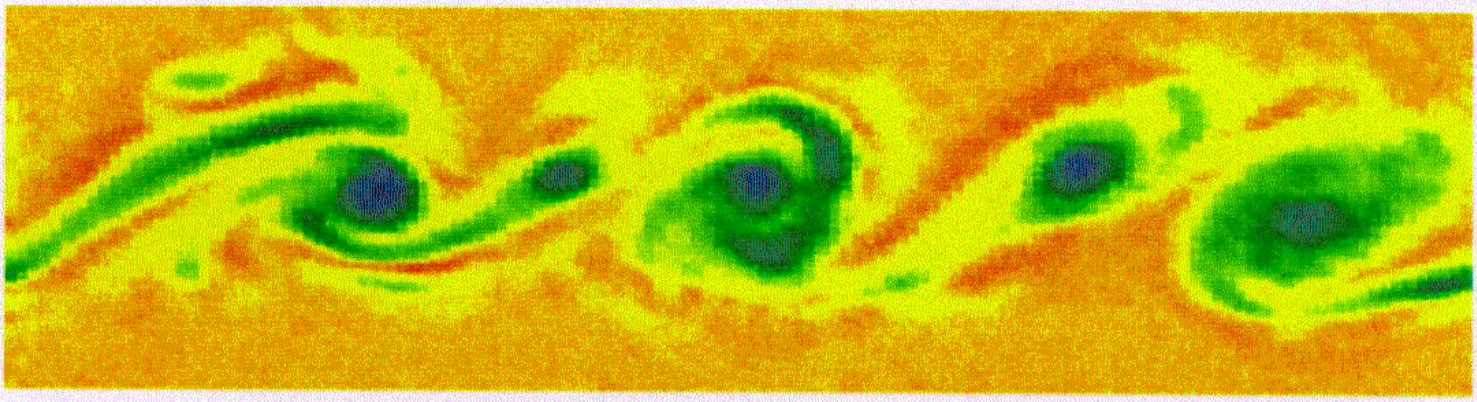

(a) −650 150 1/sec

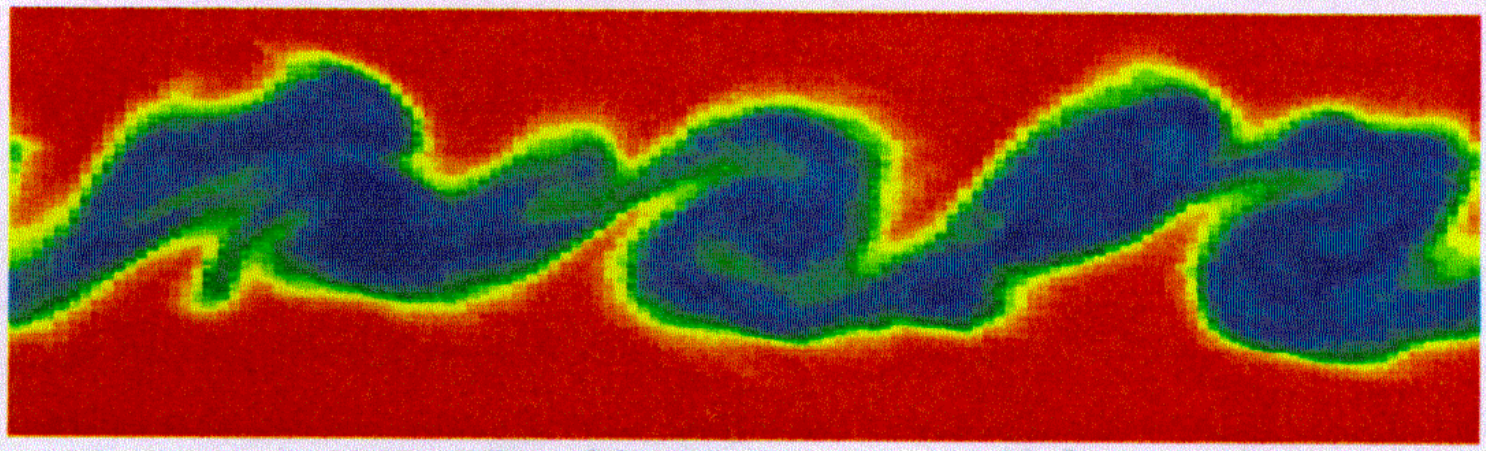

(b) .28 1.1 kg/m^3

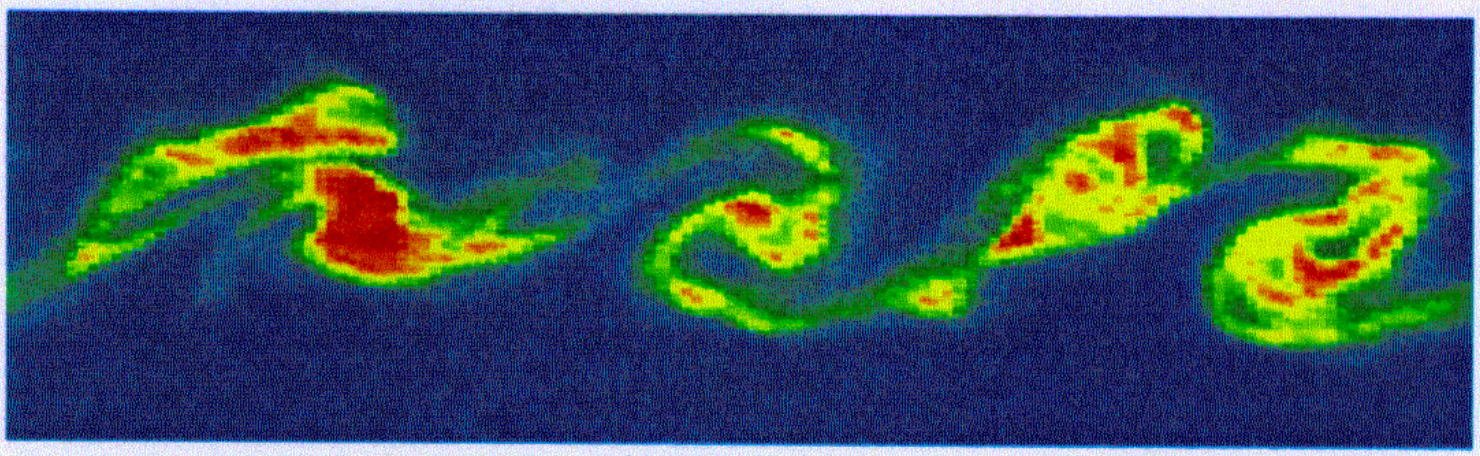

(c) 300 1100 K

Figure 6. Contours of filtered (a) vorticity, (b) subgrid density and (c) subgrid temperature at $\tau = 11$ for $\phi = 1$, $\Delta T_{fl} = 900\ K$ and no baroclinic torque effects.

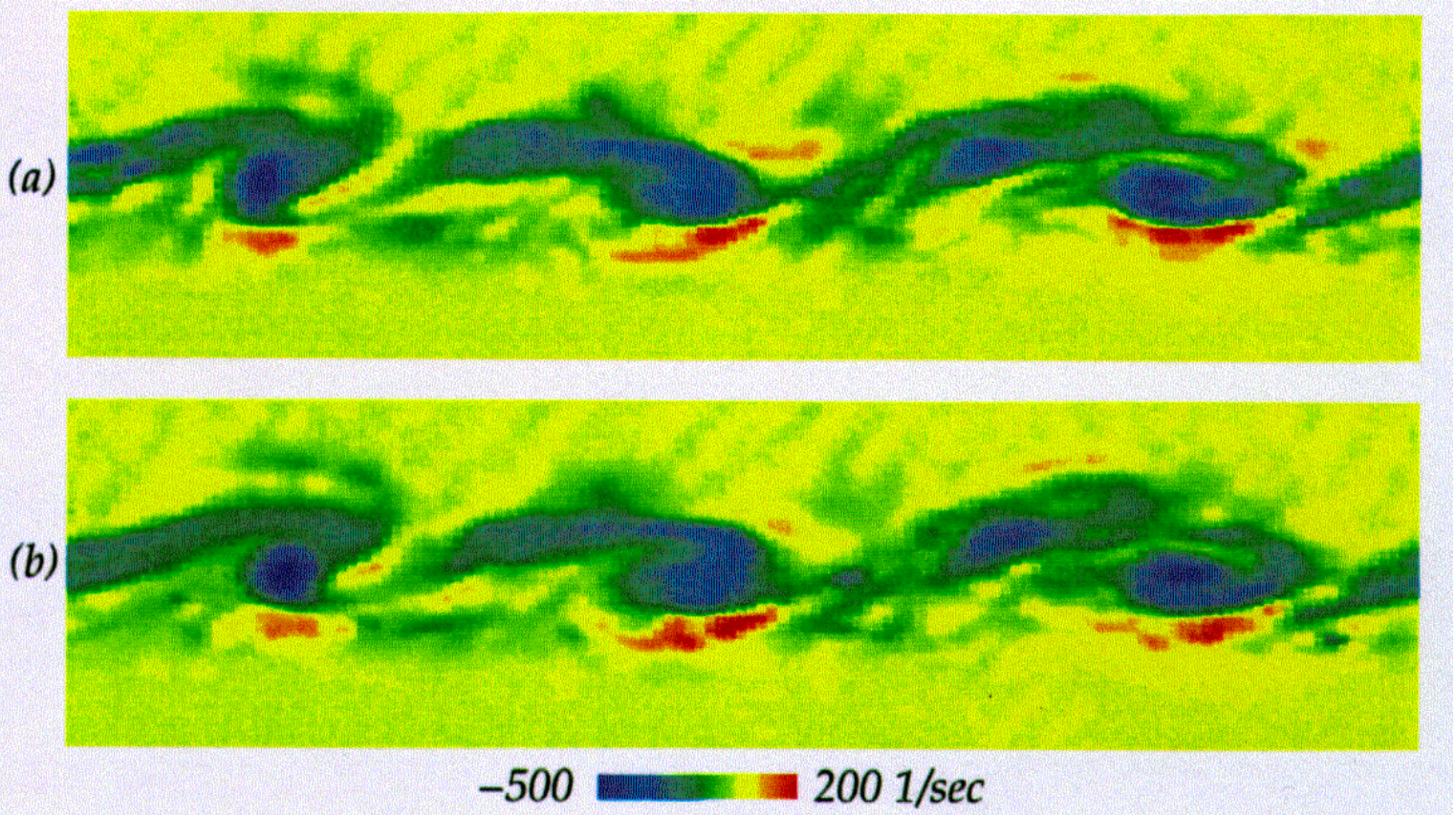

Figure 16. Filtered vorticity contours at $\tau = 11$ for pure fuel and oxidizer freestreams. (a) $\Delta T_{fl} = 450\ K$; (b) $\Delta T_{fl} = 900\ K$.

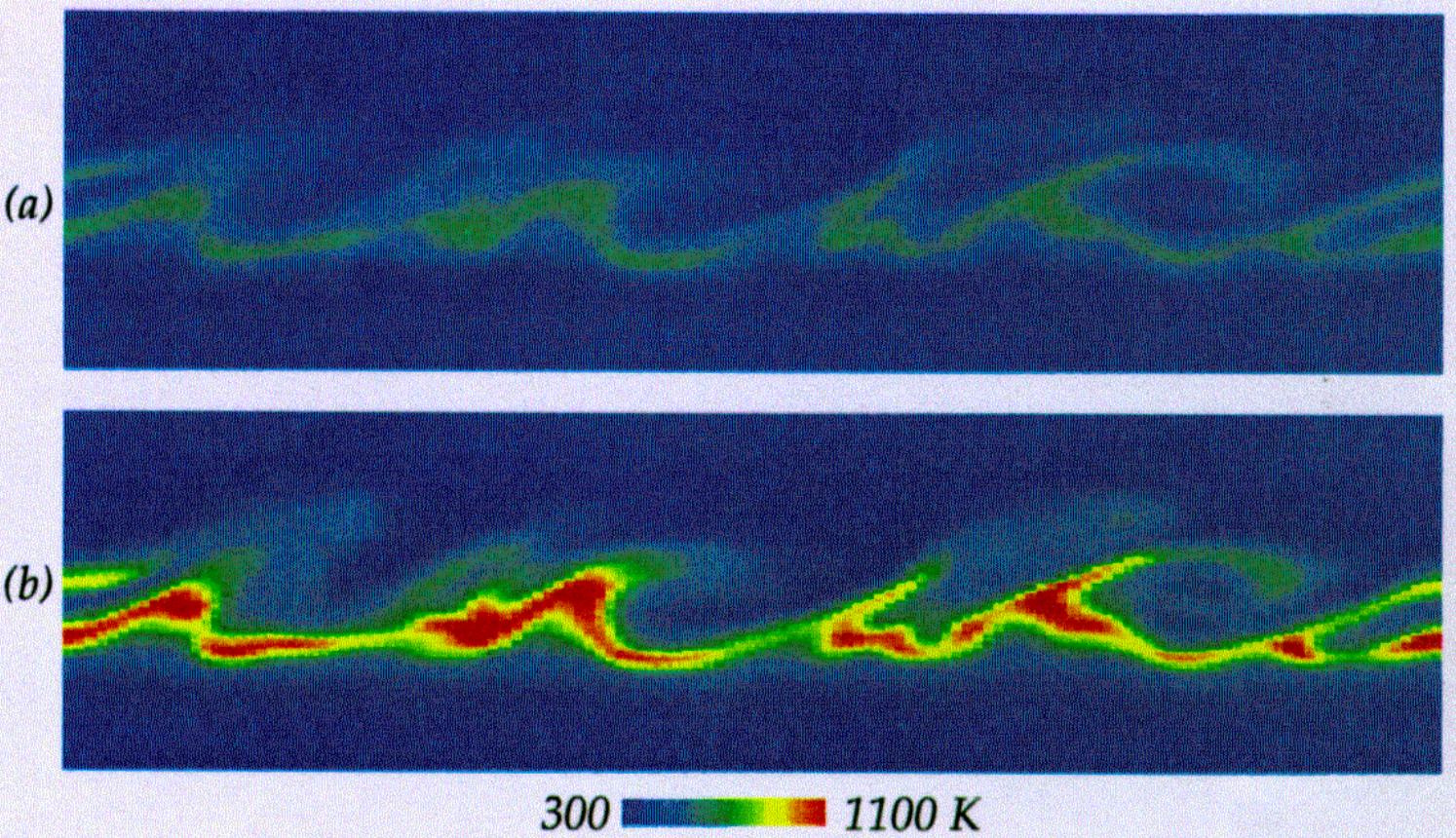

Figure 17. Filtered subgrid temperature contours at $\tau = 11$ for pure fuel and oxidizer freestreams.
(a) $\Delta T_{fl} = 450\ K$; (b) $\Delta T_{fl} = 900\ K$.

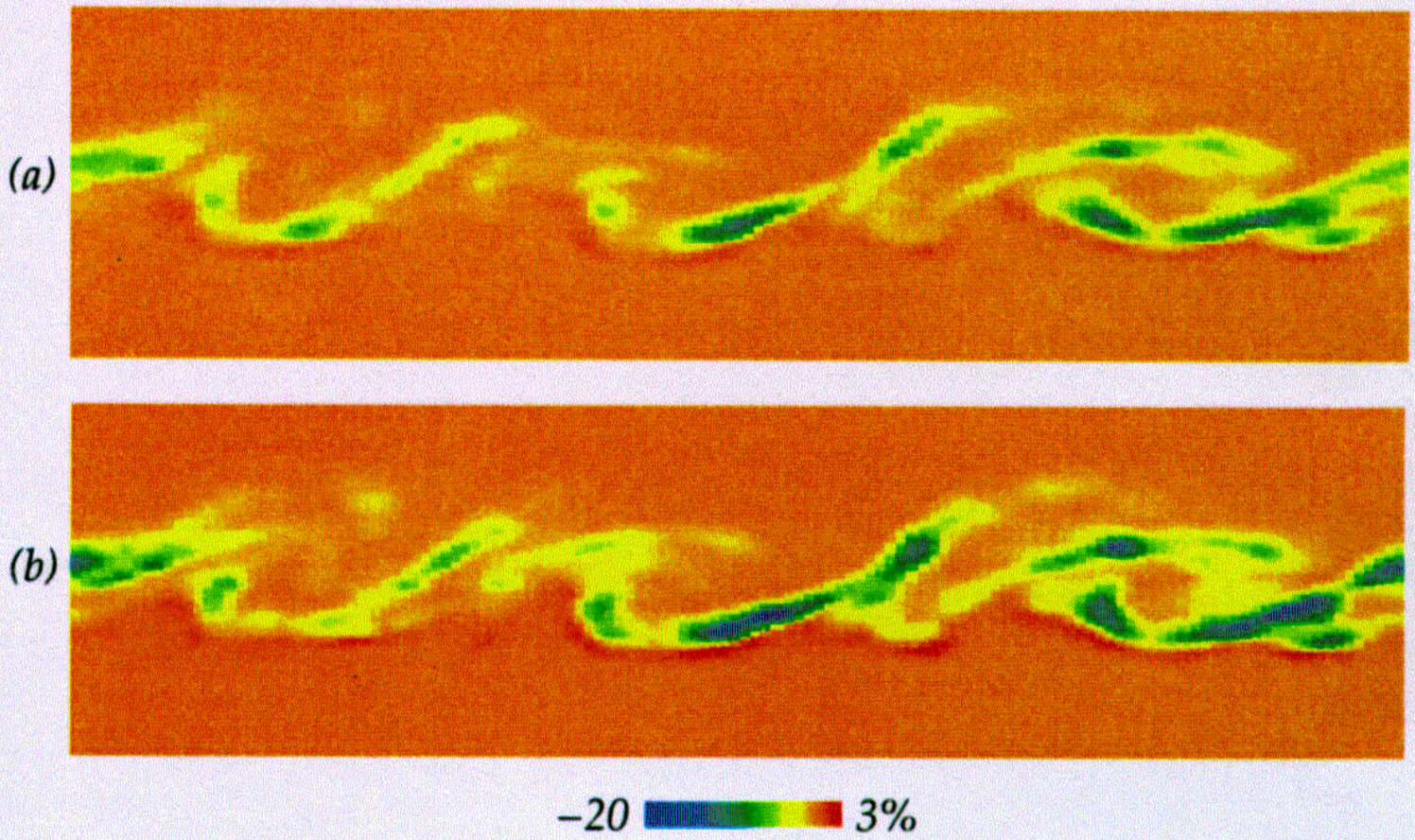

Figure 18. Contours of normalized cumulative subgrid temperature–species correlations, Λ^*/Λ^*_o, at $\tau = 11$ for pure fuel and oxidizer freestreams.
(a) $\Delta T_{fl} = 450\ K$; (b) $\Delta T_{fl} = 900\ K$.